

Article

# Control Scheme of a Concentration Photovoltaic Plant with a Hybrid Energy Storage System Connected to the Grid

Pedro Roncero-Sánchez <sup>1,\*</sup> , Alfonso Parreño Torres <sup>2</sup> and Javier Vázquez <sup>1</sup>

<sup>1</sup> School of Industrial Engineering, University of Castilla-La Mancha, Campus Universitario S/N, 13071 Ciudad Real, Spain; Javier.Vazquez@uclm.es

<sup>2</sup> Institute of Industrial Development, Castilla-La Mancha Science and Technology Park, Paseo de la Innovación 1, 02006 Albacete, Spain; alfonso.parreno@pctclm.com

\* Correspondence: pedro.roncero@uclm.es; Tel.: +34-926-295-300

Received: 26 December 2017; Accepted: 25 January 2018; Published: 30 January 2018

**Abstract:** In the last few decades, renewable energy sources (RESs) have been integrated into the electrical grid in order to curb the deficiency of energy owing to, among other factors, the depletion of fossil fuels and the increasing awareness of climate change. However, the stochastic nature of these sources, along with changes in levels of energy consumption, signifies that attention now needs to be paid for energy storage systems (ESSs). One of the most promising RESs is concentration photovoltaic (CPV) energy, owing to the high efficiency obtained and its sustainability regarding environmental issues. However, as CPV systems work only with direct solar radiation, they require ESSs in order to smooth the variations in the energy generated. This paper deals with the integration into the grid of a CPV plant that employs a hybrid ESS (HESS) based on ultracapacitors and batteries. The HESS allows the complete system to inject a constant active power level into the grid and thus flatten the profile of the energy generated. This goal is achieved by using a power electronic topology based on various DC–DC converters and a DC–AC converter, both of which share the same DC link. The control system is tailored in order to decouple the active-power and the reactive-power injections. Simulation results obtained using PSCAD/EMTDC (Power System Computer Aided Design/Electromagnetic Transient Direct Current) show the resulting performance of a 200 kW CPV plant with a hybrid ESS.

**Keywords:** concentration photovoltaic energy; ultracapacitor; battery; energy storage system; DC–AC converter; DC–DC converter

## 1. Introduction

Electricity generation making use of renewable energy sources (RESs) has a huge potential as a clean means to produce energy [1]. Nevertheless, it also behaves in a variable and discontinuous manner [2] that is usually difficult to predict, particularly in the long term. The electrical grid system is not able to store large quantities of energy by itself, and stable operation can, therefore, only be achieved by matching generation with demand [3]. Large amounts of unscheduled power fluctuation owing to RESs have become an important and challenging issue for grid operators, and it might consequently not be possible to inject all the energy generated by renewable sources into the grid [4].

Energy storage systems (ESSs) have the ability to absorb the power variations inherent to RESs [5] and can, therefore, smooth the RES power profile injected into the grid. In this context, ESSs are gaining relevance and becoming an enabling technology by which to drive the transition from a traditional and centralized energy model with a high dependence on fossil fuels towards a new paradigm based on distributed generation systems (DGSs), with an increasing presence of renewable energies, without compromising the reliability and stability of the overall electrical system.

Photovoltaic (PV) energy is one of the most promising RESs and attained a world-wide installed capacity of solar PV power generation of 177 GW by the end of 2014 [6]. One of the specific technologies of the PV system is concentration PV (CPV) energy, which employs multi-junction solar cells together with an optical system and mechanical trackers in order to obtain high conversion efficiencies [7,8], with low cost designs and long-term reliability [9]. However, CPV generators transform only direct solar radiation into electricity, owing to the reduced acceptance angle of the optical systems that they incorporate, and they are unable to capture most of the diffuse radiation [10]. The operation resulting from this feature is characterized by an on–off behaviour on cloudy days with fast transitions in the output power. The benefits of using energy storage are, therefore, evident in the particular case of CPV systems, and the integration of CPV systems with an EES may consequently contribute to reducing power variations, thus providing a smoother power profile and improving the availability of energy. Moreover, in the particular case of CPV/PV energy, new trends and policies have been proposed in order to provide these systems with other functionalities, such as power quality services, transient stability, regulation services, spinning reserves, and so forth, which implies integration with ESSs [3,11].

In the case of PV systems, low-frequency components together with high-frequency oscillations are present in the energy generated [12], and an appropriate ESS is, therefore, required. A wide variety of ESS technologies are currently available, which are usually classified into four categories: mechanical, electrical, thermal and chemical technologies [13]. After carrying out a comprehensive review of the existing storage technologies [14], it has been concluded that one of the most suitable solutions for PV energy is the use of a hybrid ESS (HESS) comprising batteries and ultracapacitors: batteries are able to store large amounts of energy, but their time response is not sufficiently rapid to cope with the transient peaks [15]. Although ultracapacitors have a low storage capacity [15], they can deliver large power peaks and can be charged and discharged without losing efficiency for thousands of cycles. Both technologies can, therefore, be combined in order to add the high energy density of the batteries to the high power density of the ultracapacitors [12,15,16]. This HESS consequently ensures a rapid transient response, a high storage capacity, easy integration and scalability.

As the HESS will store energy in DC voltage form, different DC/DC power converters will be required in order to maintain different voltage levels demanded by the system. A wide variety of power electronic topologies can be used to adapt the electrical characteristics of each device to the system requirements. In [17], several DC/DC converter schemes are analysed, including unidirectional and bidirectional topologies; although the multiple bidirectional DC/DC converter configuration can be expensive, it allows the energy exchange between ultracapacitors and battery banks; an independent control of each ESS [16,18]; and the best control action, owing to its flexibility [19].

The control scheme must be able to control the power electronic converters in order to coordinate the power exchanged between the ESS, the CPV panels and the grid. This scheme has to generate the operating modes and the reference values to properly control each power converter. Different control schemes can be found for HESS systems: one of the most usual alternatives is the use of proportional-integral (PI) controllers [17,18]. However, other control configurations can be used: in [20], a control scheme based on a Lyapunov function is employed to control the voltage of the DC-link of HESSs in electric vehicles, and a sliding mode regulator deals with the control of the currents of the batteries and ultracapacitors. Furthermore, a comparison between different control strategies, namely, a rule-based controller, a filtration-based control scheme, a model predictive controller and a fuzzy logic scheme, is shown in [19], in order to analyse their performances in a HESS for electric vehicles.

This paper deals with the integration of a CPV plant that includes a HESS into the grid. The CPV plant is tailored to inject up to 200 MW into the grid, and includes 10 identical CPV trackers, which can generate up to 25 MW. Each CPV generator is connected by means of multiple bidirectional DC/DC converters to a HESS composed of batteries and ultracapacitors, and these are connected to the grid by means of a three-phase inverter. The paper is focused on the design of the complete control system of

the CPV plant using a hierarchical topology with nested control structures. Unlike other references, which employ open-loop schemes for the energy management system, a control-loop scheme is used in this work. This scheme guarantees that the active power injected into the grid by the CPV plant is equal to the set-point value in steady state. Furthermore, a low-pass filter with an additional delay is used to reduce the supply or absorption of power by the batteries in situations of high peaks of power. The ancillary service of the injection of reactive power into the grid by the CPV plant is also considered in this paper.

The paper is organized as follows. The configuration of the CPV plant is presented in Section 2, along with the models of the ESS elements. The energy management for the ESS and the topology of the complete control system are explained in Section 3, including the various control subsystems, which are the control schemes of the batteries and the ultracapacitors, the control system of the voltage of the DC-link, and the controller for the grid-connected converter. Comprehensive simulation results of a 200 MW CPV power plant obtained with PSCAD/EMTDC are presented in Section 4. Finally, Section 5 gives the main conclusions of this work.

## 2. Configuration of the CPV Plant with a Hybrid Energy Storage System

The grid-connected CPV plant considered in this paper contains a general number of  $n$  trackers ( $CPV_1, CPV_2, \dots, CPV_n$ ) connected to the point of common coupling (PCC), and each tracker is associated with a HESS composed of ultracapacitors and batteries. Figure 1 shows the general scheme of each individual tracker.

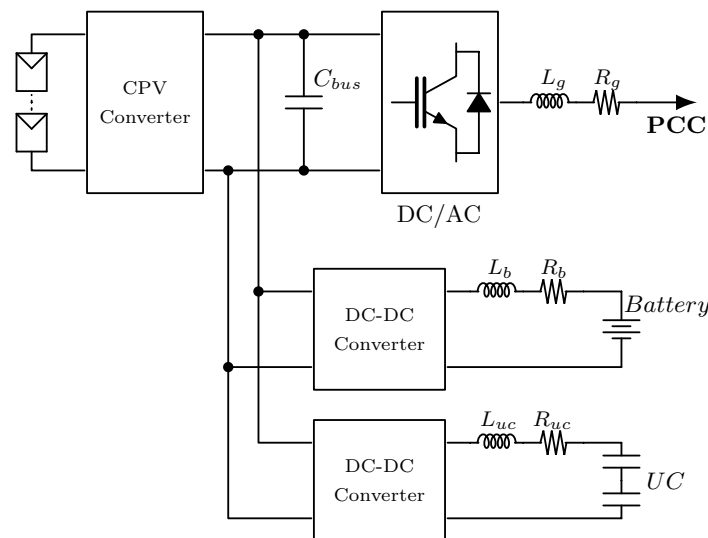


**Figure 1.** General structure of a concentration photovoltaic (CPV) tracker with hybrid energy storage system (HESS).

There are several possibilities for the HESS topology: the simplest solution is to connect the batteries and the ultracapacitors in parallel, but its main drawback is the poor use of the energy stored in the ultracapacitors, owing to the low-rated value of the battery voltage. The performance of a HESS is normally improved by means of power electronic converters, as these decouple the operation of each storage element [21].

Figure 2 shows the detailed configuration of the proposed HESS for each one of the CPV trackers of the PV plant. It consists of the CPV modules, a grid-connected converter and the HESS system, which is composed of a set of batteries and a bank of ultracapacitors. All the converters share the capacitor  $C_{bus}$ , whose voltage is maintained at a necessary level by an appropriate control scheme for the correct operation of the complete system. This capacitor is usually called the DC-link, as all the converters are connected to it.

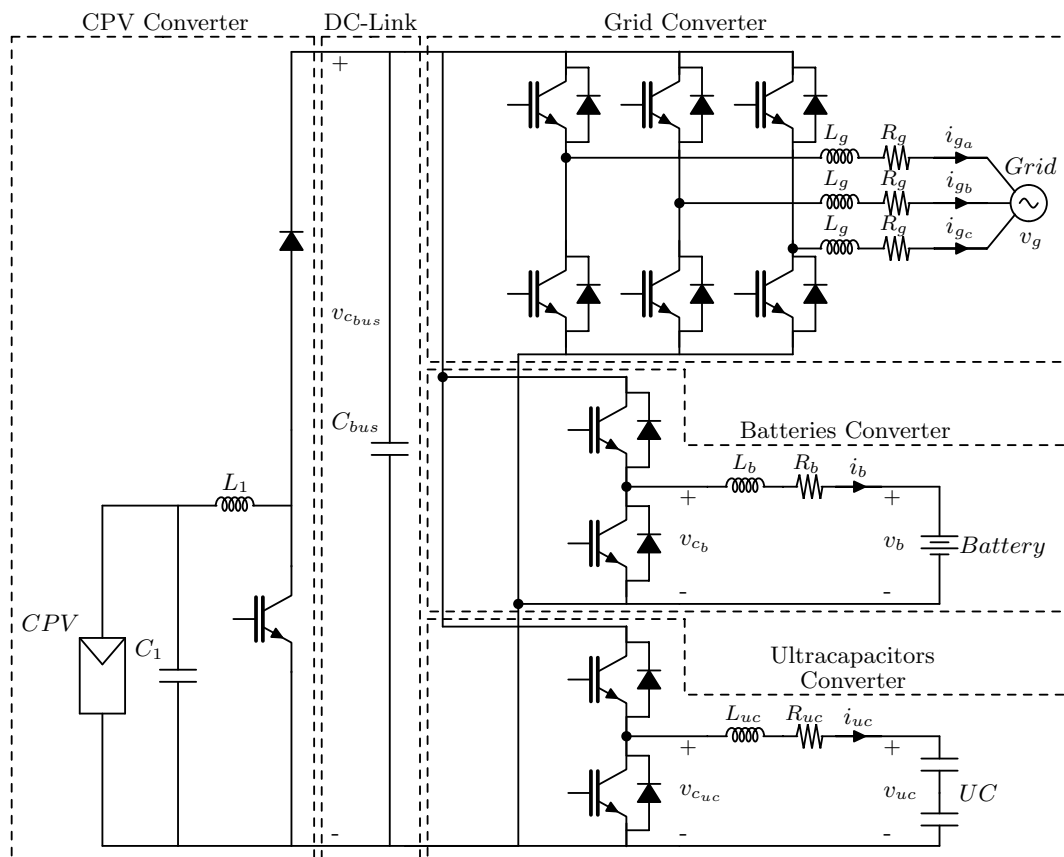


**Figure 2.** Detailed scheme of the hybrid energy storage system (HES) for a concentration photovoltaic (CPV) panel.

The CPV converter is a boost unidirectional converter, and its goal is to maximise the power generated by the CPV modules by modifying the operating point. The converter must, therefore, include the functionality of maximum power point tracking (MPPT).

The grid-connected converter is a two-level voltage source converter (VSC), which is responsible for injecting the active power generated and compensating for the necessary reactive power. In this work, the VSC is connected to the grid via an inductive filter ( $L_g - R_g$ ), owing to its simplicity, although there are other alternatives, such as the use of inductive-capacitive-inductive (LCL) filters [22].

Two half-bridge bidirectional converters allow the batteries and the ultracapacitors to exchange power with the grid and the CPV modules. These converters maintain the output voltage, while the output current can flow in both directions. This means that the batteries and the ultracapacitors can either generate or store energy [23]. Furthermore, the batteries and the ultracapacitors are connected to their respective converters by means of inductive filters; that is,  $L_b - R_b$  for the batteries and  $L_{uc} - R_{uc}$  for the ultracapacitors.

It should be noted that the power electronic converters are operated with a sufficiently high switching frequency, which implies that they can be considered as linear amplifiers [24,25].

### 2.1. Model of the CPV Modules

Although the main objective of this work is not to focus on the CPV module or its associated DC/DC converter, it is useful to know the main features and a basic model of the CPV modules.

The model of the PV cell is well known and is usually based on the model of a single diode [26]. CPV systems normally use multi-junction cells and optical lenses to concentrate sunbeams onto the PV cell in order to increase efficiency, although their model can also be analogous to the conventional solar cells. The electrical behaviour of a CPV module can, therefore, be approximated by the solar

cell with series and shunt resistance [27], which is shown in Figure 3: a forward-biased diode with an ideality factor  $m$  models the recombination of electrons inside the cell and is connected in parallel with the current generator  $I_{ph}$ , which is the photogenerated current. The voltage and the current generated by the CPV module are  $V_{pv}$  and  $I_{pv}$ , respectively, whereas the resistances  $R_p$  and  $R_s$  model the electrical losses.

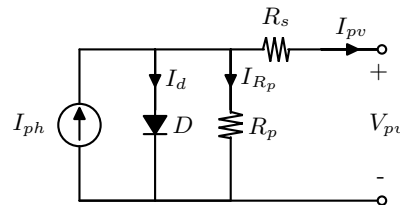


**Figure 3.** Electrical model for concentration photovoltaic (CPV) modules.

The output current of the CPV module can be calculated as  $I_{pv} = I_{ph} - I_d - I_{R_p}$ , where the diode current is calculated as follows:

$$I_d = I_{osc} \left( e^{\frac{q(V_{pv} + R_s I_{pv})}{mKT}} - 1 \right) \quad (1)$$

where  $I_{osc}$  is the dark current of the diode,  $K$  is the Boltzman constant,  $T$  is the temperature and  $q$  is the electron charge.

The current through the resistance  $R_p$  is

$$I_{R_p} = \frac{V_{pv} + I_{pv} R_s}{R_p} \quad (2)$$

As the operating point of the CPV module is usually set close to the maximum power point (MPP) by the CPV converter [28], and because the PV generator can be seen as a current source with limited output voltage and power [29], the CPV modules and the CPV converter are modelled as a current source in the remainder of the paper.

## 2.2. Model of the Batteries

Batteries based on lead–acid technology are usually employed in PV applications owing to several factors: this is a mature technology with a high degree of reliability, and the weight and the volume are not critical constraints in PV plants.

A variety of electrical equivalent circuits can emulate the performance of lead–acid batteries. The Thévenin model provides a good equilibrium between the degree of complexity and high accuracy in short time periods and during transients [30]. Several combinations of resistances and capacitors can be considered. However, a single resistive-capacitive (RC) branch can be assumed to be sufficiently accurate, as shown in Figure 4. Thus,  $R_{b_p}$  represents the chemical resistance of the battery, and  $C_{b_p}$  represents the accumulative effect of the charging process. An internal series resistance  $R_{b_s}$  with which to connect one cell to another also needs to be taken into account. These values are, to some extent, dependent on the state of charge (SOC) and on the temperature of the battery. The SOC expresses the percentage of energy that the battery has accumulated. The open-circuit voltage  $V_{OC}$ , which can be measured in the battery when no load is connected, is the first parameter that changes according to the SOC, supplying a different output voltage while it is charging or discharging. This is the internal voltage that the battery has at any time owing to the energy stored with the internal chemical reactions.

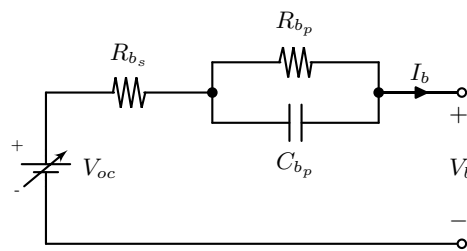


Figure 4. Thévenin model of a battery with a single branch.

According to Figure 4, the transfer function of the impedance of the battery can be obtained as

$$Z_b(s) = \frac{V_b(s)}{I_b(s)} = R_{b_s} + \frac{R_{b_p}}{1 + R_{b_p} C_{b_p}} \quad (3)$$

where  $V_b(s)$  and  $I_b(s)$  are the output voltage and the output current of the battery, respectively.

Furthermore, the state-variable model of the connection filter of the bank of batteries can, as shown in Figure 2, be written as

$$\frac{di_b}{dt} = -\frac{R_b}{L_b} i_b + \frac{1}{L_b} v_{c_b} - \frac{1}{L_b} v_b \quad (4)$$

where the parameters  $L_b$  and  $R_b$  are the inductance and the stray resistance, respectively, of the connection filter between the bank of batteries and the DC–DC converter, and  $v_{c_b}$  is the output voltage of the DC–DC converter.

Equation (4) can alternatively be written in the Laplace domain as

$$I_b(s) = \frac{V_{c_b}(s)}{L_b s + R_b} - \frac{V_b(s)}{L_b s + R_b} \quad (5)$$

Although the model presented in this paper does not take the battery degradation into account, previous works have proposed a dynamic degradation model that can be used to prolong the service life of the battery [19].

### 2.3. Model of the Ultracapacitors

The capacity of ultracapacitors is much higher than that of conventional capacitors owing to the fact that their electrodes are made of a porous material, which provides an effective surface that is larger than that of classical capacitors.

Several models can be used to describe the dynamical behaviour of an ultracapacitor, as explained in [31,32]. Of these, the simplest approach is the first-order RC model shown in Figure 5, which contains an equivalent series resistance  $R_{ucs}$ , the capacitance  $C_{uc}$  and a parallel resistance  $R_{ucp}$  that models the self-discharge of the ultracapacitor. Unlike conventional capacitors, in the case of ultracapacitors, their capacitance depends on the voltage applied [33].

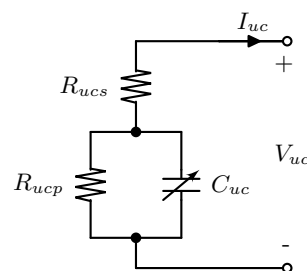


Figure 5. Electrical equivalent model for ultracapacitor.

The transfer function of the impedance of the ultracapacitor can be calculated as

$$Z_{uc}(s) = \frac{V_{uc}(s)}{I_{uc}(s)} = R_{ucs} + \frac{R_{ucp}}{1 + R_{ucp}C_{uc}} \quad (6)$$

where  $I_{uc}(s)$  is the current through the ultracapacitors and  $V_{uc}(s)$  is voltage across the ultracapacitors.

As in the case of the batteries, the current  $I_{uc}(s)$  can be obtained in the Laplace domain as follows (see Figure 2):

$$I_{uc}(s) = \frac{V_{cuc}(s)}{L_{uc}s + R_{uc}} - \frac{V_{uc}(s)}{L_{uc}s + R_{uc}} \quad (7)$$

where the parameters  $L_{uc}$  and  $R_{uc}$  are the inductance and the stray resistance, respectively, of the connection filter between the bank of ultracapacitors and the DC–DC converter, and  $V_{cuc}$  is the converter output voltage.

#### 2.4. Model of the Grid-Connected Converter

The single-phase equivalent circuit of the grid-connected converter plotted in Figure 2 is shown in Figure 6, in which the VSC is connected to the grid via an inductive filter and is modelled as an ideal voltage source  $u$ . The parameters  $L_g$  and  $R_g$  represent the inductance and the stray resistance, respectively, of the grid-connection filter, while  $i_g$  is the current injected into the grid and  $v_g$  is the grid voltage at the PCC.

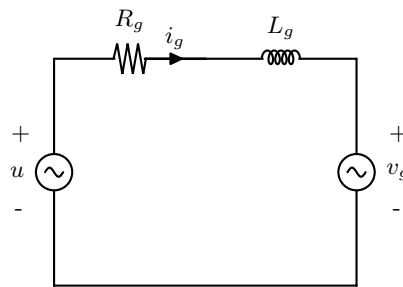


**Figure 6.** Single-phase equivalent circuit of the grid-connected converter.

In accordance with Figure 6, and if a three-leg converter is used, the state-variable model of the complete three-phase system  $\{A, B, C\}$  is

$$\frac{d}{dt} \begin{bmatrix} i_{gA} \\ i_{gB} \\ i_{gC} \end{bmatrix} = \begin{bmatrix} -\frac{R_g}{L_g} & 0 & 0 \\ 0 & -\frac{R_g}{L_g} & 0 \\ 0 & 0 & -\frac{R_g}{L_g} \end{bmatrix} \begin{bmatrix} i_{gA} \\ i_{gB} \\ i_{gC} \end{bmatrix} + \frac{1}{L_g} \begin{bmatrix} 1 & 0 & 0 \\ 0 & 1 & 0 \\ 0 & 0 & 1 \end{bmatrix} \begin{bmatrix} u_A - v_{gA} \\ u_B - v_{gB} \\ u_C - v_{gC} \end{bmatrix} \quad (8)$$

Furthermore, the use of Park's transformation enables the state-variable model of the inductive filter to be expressed in a reference frame that rotates at the fundamental frequency  $\omega_1$  and is usually called the synchronous reference frame (SRF). The use of the SRF allows the  $q$  component of the grid voltage to be zero and the sinusoidal magnitudes to become DC variables [34]. The following state-variable model of the grid-connected converter is obtained when the SRF is employed [35]:

$$\frac{d}{dt} \begin{bmatrix} i_{gd} \\ i_{gq} \end{bmatrix} = \begin{bmatrix} -\frac{R_g}{L_g} & \omega_1 \\ -\omega_1 & -\frac{R_g}{L_g} \end{bmatrix} \begin{bmatrix} i_{gd} \\ i_{gq} \end{bmatrix} + \frac{1}{L_g} \begin{bmatrix} 1 & 0 \\ 0 & 1 \end{bmatrix} \begin{bmatrix} u_d - v_{gd} \\ u_q \end{bmatrix} \quad (9)$$

where  $i_{gd}$  and  $i_{gq}$  are the  $d$  and  $q$  components of the current  $i_g$ , respectively;  $u_d$  and  $u_q$  are the  $d$  and  $q$  components of the output voltage of the grid-connected converter; and  $v_{gd}$  is the  $d$  component of the grid voltage  $v_g$ .

Although the state-variable model (Equation (9)) is coupled, a decoupled equivalent system can be obtained for control purposes, as explained in [34]. Furthermore, if an invariant-power Park's transformation is chosen, the active power,  $p_g$ , and the reactive power,  $q_g$ , injected into the grid can be calculated in the SRF as follows:

$$p_g = v_{gd} i_{gd} \quad (10)$$

$$q_g = -v_{gd} i_{gq} \quad (11)$$

### 2.5. Model of the DC-Link

The power generated by the CPV system  $p_{cpv}$  must be equal to the power injected into the grid,  $p_g$ , plus the power exchanged with the batteries  $p_b$ , ultracapacitors  $p_{uc}$  and the capacitor  $C_{bus}$  of the DC-link,  $p_{C_{bus}}$ , plus the power losses  $p_{loss}$  owing to the connection filters and the losses of the semiconductors. This can be written as

$$p_{cpv} = p_{C_{bus}} + p_g + \overbrace{p_b + p_{uc}}^{p_{st}} + p_{loss} \quad (12)$$

It should be noted that a positive sign of the power indicates that the power flows into the device, that is, the batteries, grid, and so forth, whereas a negative sign refers to the power being extracted from the device. Moreover, the sum of the power of the batteries and that of the ultracapacitors is the power of the ESS  $p_{st}$ , and the power of the DC-link capacitor can be calculated as

$$p_{C_{bus}} = i_{C_{bus}} v_{C_{bus}} = C_{bus} \frac{dv_{C_{bus}}}{dt} v_{C_{bus}} = \frac{C_{bus}}{2} \frac{d(v_{C_{bus}})^2}{dt} \quad (13)$$

where  $i_{C_{bus}}$  is the current injected into the DC-link capacitor and  $v_{C_{bus}}$  is the voltage of the DC-link.

If the voltage  $v_{C_{bus}}$  remains constant, the DC-link does not absorb or generate power, as shown in Equation (13), and all the power generated by the CPV panels will, therefore, be transferred to the grid and the energy storage elements, that is, the batteries and the ultracapacitors.

## 3. Energy Management and Topology of the Control System

In this paper, the objective of the energy management system is to maintain a constant profile of the power injected into the grid, thus avoiding the inherent variations of the CPV panels. Furthermore, during the initial and final time intervals of energy generation, the power profile will be programmed with a ramp: the power injected will be increased at the beginning, whereas the power injected into the grid will decrease at the end of the generation interval. This is the behaviour of conventional PV panels, in which the power output increases in the early morning and decreases in the late afternoon.

Moreover, the control system is able to compensate for the reactive power according to, for example, the requirements of the grid operator.

We let  $P_g^*$  and  $Q_g^*$  be the references of the active and reactive powers that the CPV plant exchanges with the grid. If  $n_{cpv}$  is the number of trackers of the CPV plant, the references of the active and reactive powers between each tracker and the grid can therefore be obtained as  $p_g^* = P_g^*/n_{cpv}$  and  $q_g^* = Q_g^*/n_{cpv}$ , respectively.

The reference for the power of the ESS,  $p_{st}^*$ , can be obtained through the implementation of several solutions. One of the most extended methods involves calculating this reference as  $p_{st}^* = p_g^* - p_{cpv}$  [12,36]. This solution is very simple and is based on an open-loop scheme. However, the power losses of the connection filters are not taken into account, and differences can be expected between the reference of the active power and the true value.

In this paper, we propose to resolve this issue through the use of a solution based on a closed-loop configuration, as shown in Figure 7.

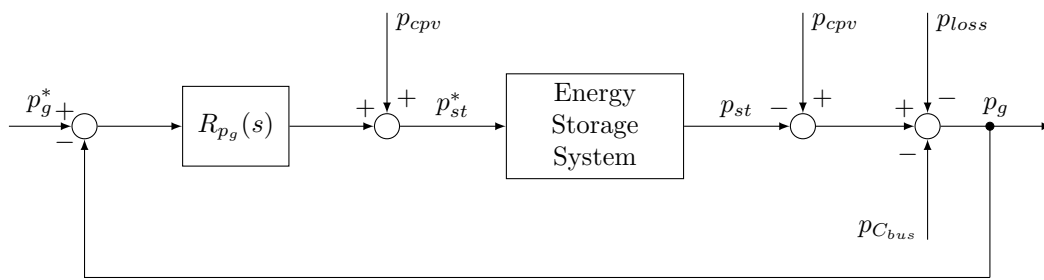


Figure 7. Closed-loop scheme for the control of the active power injected into the grid.

This closed-loop configuration employs an integral action  $R_{p_g}(s)$ , which guarantees zero-tracking error in steady state for step changes in the set point, that is, when the input  $p_g^*$  is constant, with the transfer function:

$$R_{p_g}(s) = \frac{k_{p_g}}{s} \tag{14}$$

The design of Equation (14) must be carried out in such a way that the dynamics of  $p_g$  are much slower than the dynamics of the control loop of the ESS. This assumption implies that the ESS dynamics can be approximated by unity when compared with the dynamics of the output system  $p_g$ , which implies that  $p_{st} \approx p_{st}^*$ . Furthermore, as the power of the CPV system  $p_{cpv}$  is a disturbance that can be measured, a feed-forward action of  $p_{cpv}$  is added to completely compensate for its effect, as shown in Figure 7. The power injected into the grid can, therefore, be obtained as

$$p_g(s) = -\frac{R_{p_g} p_g^*(s)}{1-R_{p_g}(s)} - \frac{p_{loss}(s)}{1-R_{p_g}(s)} - \frac{p_{C_{bus}}(s)}{1-R_{p_g}(s)} = \frac{-k_{p_g}}{s-k_{p_g}} p_g^*(s) - \frac{s}{s-k_{p_g}} p_{loss}(s) - \frac{s}{s-k_{p_g}} p_{C_{bus}}(s) \tag{15}$$

Equation (15) shows that  $p_g(0) = p_g^*(0)$ ; that is, the output is equal to the reference when the reference is constant. Moreover, the closed-loop system is a first-order system that is stable for any negative value of  $k_{p_g}$  and is not dependent on the disturbance  $p_{cpv}$ .

The complete control structure is a hierarchical control scheme, for which the configuration plotted in Figure 7 is the top-level scheme. Having presented this scheme, we now go on to explain the remaining control schemes.

### 3.1. Control System of the ESS

The reference for the power of the ESS,  $p_{st}^*$ , must be split into the reference for the power of the batteries  $p_b^*$  and the reference for the power of the ultracapacitors  $p_{uc}^*$ , that is,  $p_{st}^* = p_b^* + p_{uc}^*$ . It is well known that the energy generated by solar panels contains a low-frequency component and high-frequency oscillations associated with the intermittent solar irradiance [12]. The batteries should, therefore, be used to deal with the low-frequency component, whereas the ultracapacitors should provide and absorb the transient power peaks [16]. This can be achieved by using a low-pass filter  $H_{st}(s)$ , which separates the low-frequency component associated with the batteries from the high-frequency component related to the ultracapacitor bank, as shown in Figure 8.

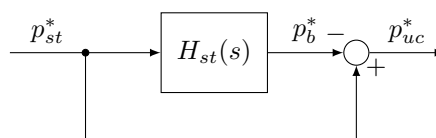
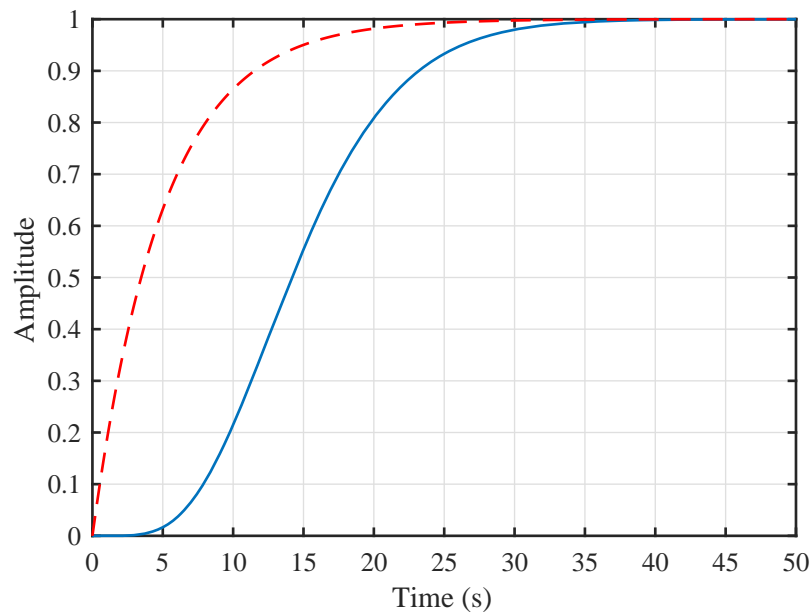


Figure 8. Calculation of the power references for the batteries  $p_b^*$  and the ultracapacitors  $p_{uc}^*$ .

The filter used to generate  $p_b^*$  is usually a first-order low-pass filter [12], which can smooth the power profile required for the batteries. However, in some cases, the initial value of the power of the ESS may be very high, and a first-order filter is not sufficient to limit that initial value. In this paper,

a second-order filter to the power of  $n_f$  is proposed ( $n_f$  being a positive integer greater than 1). This filter establishes a delay in its time response, thus avoiding the supply or absorption of power by the batteries; instead of this, the ultracapacitors deal with the power required. The filter is, therefore, defined as  $H_{st}(s) = H_2(s)^{n_f}$ , and, as an example, Figure 9 shows a comparison of a first-order low-pass filter with the solution proposed in this paper, for which a second-order filter with  $n_f = 3$  is used. It is noted that this solution establishes an initial delay of approximately 3.5 s and that the time response is smoother than that obtained with the first-order approach.



**Figure 9.** Step responses for the power reference for the batteries  $p_b^*$  obtained with  $H_{st}(s) = \left(\frac{0.16}{s^2+0.8s+0.16}\right)^3$  (blue —) and  $H_{st}(s) = \frac{0.2}{s+0.2}$  (red - -).

The converters associated with the batteries and the ultracapacitors are controlled using a current-control loop. Under the assumption that the voltages of the batteries and the ultracapacitors change very slowly when compared to their respective currents, the references for the currents of the batteries and the ultracapacitors can, therefore, be calculated as follows:

$$I_b^*(s) = \frac{p_b^*(s)}{V_b(s)} \quad (16)$$

$$I_{uc}^*(s) = \frac{p_{uc}^*(s)}{V_{uc}(s)} \quad (17)$$

These references are subsequently compared with the measured currents, that is,  $I_b(s)$  and  $I_{uc}(s)$ , and the differences are driven to two PI-type regulators, as shown in Figure 10. Furthermore, a feed-forward action is used in order to cancel out the effect of the voltages of the batteries and the ultracapacitors in their respective control systems. Finally, each control system generates the reference required for the output voltage of the respective DC–DC converter. This voltage reference is employed in a pulse-width modulation (PWM) scheme to generate the firing signal of the converter.

As shown in Figure 10a,b, and taking into account Equations (5) and (7), the following closed-loop transfer functions are obtained for the control of the current of the batteries and the current of the ultracapacitors:

$$F_{i_b}(s) = \frac{I_b(s)}{I_b^*(s)} = \frac{k_{p_b}s + k_{i_b}}{L_b s^2 + (k_{p_b} + R_b)s + k_{i_b}} = \frac{p_b(s)}{p_b^*(s)} \quad (18)$$

$$F_{i_{uc}}(s) = \frac{I_{uc}(s)}{I_{uc}^*(s)} = \frac{k_{p_{uc}}s + k_{i_{uc}}}{L_{uc}s^2 + (k_{p_{uc}} + R_{uc})s + k_{i_{uc}}} = \frac{p_{uc}(s)}{p_{uc}^*(s)} \quad (19)$$

Moreover, as  $p_{st}(s) = p_b(s) + p_{uc}(s)$ , the total energy of the storage system can be written as  $p_{st}(s) = F_{i_b}(s)p_b^*(s) + F_{i_{uc}}(s)p_{uc}^*(s)$ . If the control system is designed in such a way that  $F_{i_b}(s) = F_{i_{uc}}(s)$ , then  $p_{st}(s) = F_{i_b}(s) \overbrace{(p_b^*(s) + p_{uc}^*(s))}^{p_{st}^*(s)}$ . In this situation, the closed-loop transfer function of the ESS plotted in Figure 7 is, therefore,  $F_{i_b}(s)$ .

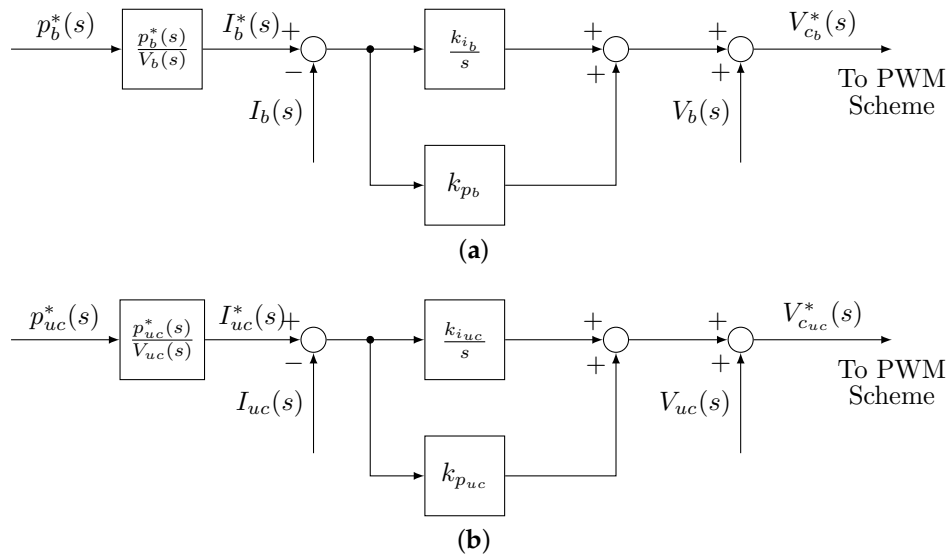


**Figure 10.** Control scheme of the DC–DC converters associated with (a) the batteries, and (b) the ultracapacitors.

### 3.2. Control System of the Voltage of the DC-Link and the Grid-Connected Converter

The voltage of the DC-link can be written by combining Equations (12) and (13) as

$$\frac{d(v_{C_{bus}})}{dt} = \frac{2}{C_{bus}} [p_{cpv} - p_g - p_{st} - p_{loss}] = \frac{2}{C_{bus}} [p_{cpv} - v_{g_d} i_{g_d} - p_{st} - p_{loss}] \quad (20)$$

Equation (20) shows that the voltage of the DC-link can be controlled by regulating the  $d$  component of the grid current,  $i_{g_d}$ , or the power of the ESS,  $p_{st}$ , as the other terms in the equation are disturbances that cannot be used for control purposes. Because the power  $p_{st}$  is employed to control the active power injected into the grid, as can be seen in Figure 7, the current  $i_{g_d}$  is used to control the voltage value of the DC-link, and the output of the regulator of this voltage is therefore the reference value for the current  $i_{g_d}$ , that is,  $i_{g_d}^*$ .

The reactive power exchanged with the grid can, according to Equation (11), also be controlled by modifying the  $q$  component of the grid current,  $i_{g_q}$ . This signifies that if the reference of the reactive power injected into the grid is  $q_g^*$ , the reference value for the current  $i_{g_q}$  can be calculated as  $i_{g_q}^* = -q_g^*/v_{g_d}$ .

The control of the voltage of the DC-link and the reactive power exchanged with the grid therefore requires an appropriate closed-loop control for the currents  $i_{g_d}$  and  $i_{g_q}$ . This control structure is designed by taking into account the state-space model (Equation (9)), which is coupled, as mentioned

in Section 2.4. In order to tackle this problem, the following decoupled model can be achieved after some calculations (see reference [34] for more details):

$$\frac{d}{dt} \begin{bmatrix} i_{gd} \\ i_{gq} \end{bmatrix} = \begin{bmatrix} -\frac{R_g}{L_g} & 0 \\ 0 & -\frac{R_g}{L_g} \end{bmatrix} \begin{bmatrix} i_{gd} \\ i_{gq} \end{bmatrix} + \frac{1}{L_g} \begin{bmatrix} 1 & 0 \\ 0 & 1 \end{bmatrix} \begin{bmatrix} w_d \\ w_q \end{bmatrix} \quad (21)$$

where  $w_d$  and  $w_q$  are fictitious variables used to decouple the model given by Equation (9). The variables  $u_d$  and  $u_q$  are calculated by using  $w_d$ ,  $w_q$ ,  $i_{gd}$  and  $i_{gq}$  according to the following decoupling equation:

$$\begin{bmatrix} u_d \\ u_q \end{bmatrix} = L_g \begin{bmatrix} 0 & -\omega_1 \\ \omega_1 & 0 \end{bmatrix} \begin{bmatrix} i_{gd} \\ i_{gq} \end{bmatrix} + \begin{bmatrix} w_d \\ w_q \end{bmatrix} + \begin{bmatrix} v_{gd} \\ 0 \end{bmatrix} \quad (22)$$

As the quantities to be controlled are DC magnitudes, one of the most popular control laws for the grid current is the PI regulator. The transfer function of this regulator  $R_{i_g}(s)$  is designed according to Equation (21) and can be written for  $d$  and  $q$  components as follows:

$$W_d(s) = k_{i_{ig}} \frac{I_{gd}^*(s) - I_{gd}(s)}{s} - k_{p_{ig}} I_{gd}(s) \quad (23)$$

$$W_q(s) = k_{i_{ig}} \frac{I_{gq}^*(s) - I_{gq}(s)}{s} - k_{p_{ig}} I_{gq}(s) \quad (24)$$

where the controller outputs are the  $d - q$  components  $W_d(s)$  and  $W_q(s)$ ;  $k_{i_{ig}}$  and  $k_{p_{ig}}$  are the integral and proportional gains, respectively.

Similarly, the controller for the voltage of the DC-link,  $R_{v_{C_{bus}}}(s)$ , is also a PI regulator and is tailored in accordance with Equation (20). The control law for  $R_{v_{C_{bus}}}(s)$  can be defined as

$$I_{gd}^*(s) = k_{i_{v_C}} \frac{V_{C_{bus}}^{*2}(s) - V_{C_{bus}}^2(s)}{s} + k_{p_{v_C}} \left( V_{C_{bus}}^{*2}(s) - V_{C_{bus}}^2(s) \right) \quad (25)$$

where  $V_{C_{bus}}^*(s)$  is the reference value for the DC-link voltage, and  $k_{i_{v_C}}$  and  $k_{p_{v_C}}$  are the integral and proportional gains of  $R_{v_{C_{bus}}}(s)$ , respectively.

Figure 11 shows the block diagram of the control scheme of the voltage of the DC-link and the grid-connected converter, for which the superscript \* represents the reference values. The output of the regulator  $R_{v_{C_{bus}}}(s)$  is the reference of the  $d$  component of the grid current, while the controllers  $R_{i_g}(s)$  provide the variables  $w_d$  and  $w_q$  needed to control the  $d - q$  components of the current injected into the grid. The decoupling Equation (22) is used to obtain the converter voltage in the SRF, and, after the inverse Park's transformation, the three-phase voltages of the converter are calculated and driven to a sinusoidal PWM scheme in order to generate the firing signals for the switches of the converter.

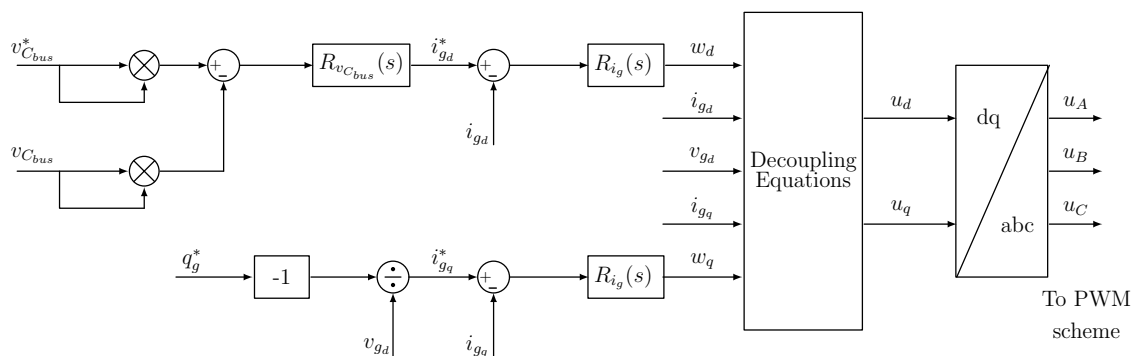


Figure 11. Control scheme of the voltage of the DC-link and the grid-connected converter.

#### 4. Simulation Results

A CPV power plant that contains various trackers such as that depicted in Figure 1 has been simulated using PSCAD/EMTDC. The CPV plant contained 10 identical trackers with hybrid energy storage units, that is,  $n = 10$ . Each tracker was able to generate a maximum power of 25 kW, and the objective was the constant injection into the grid of  $p_g^* = 20$  kW per tracker combined with its HESS, which implies that the total power injected into the grid by the CPV power plant was  $n \cdot p_g^* = 200$  kW. Furthermore, and as is explained in Section 3, in the initial period of the simulation, a linear increase in the power injected into the grid by each tracker–HESS unit with a slope of  $1/3 \text{ kW} \cdot \text{s}^{-1}$  was scheduled; that is, the reference value of 20 kW was attained after 60 s, while an equivalent linear decrease with a slope of  $-1/3 \text{ kW} \cdot \text{s}^{-1}$  was scheduled at the instant  $t = 1350$  s. In addition, the injection of reactive power with a maximum value of 5 kVAr per tracker was also scheduled in the time interval  $700 \text{ s} \leq t \leq 1000 \text{ s}$ .

The CPV power plant was connected to a 13.8 kV distribution grid by means of the primary side of a three-phase transformer with a winding ratio of 400 V/13.8 kV and a star/delta connection. Each HESS was composed of 12 batteries connected in series, with a capacity of 100 Ah and rated voltage of 12 V, and a 47 F ultracapacitor with a rated voltage of 200 V. The initial voltages of the ultracapacitors were set to 150 V.

The power converters implemented in the test employed insulated-gate bipolar transistor (IGBT) switches operated by proper PWM algorithms. Although this option implies that the simulation took place over a longer execution time, it was preferred to the use of average models of the converters, as the switching behaviour could be analysed.

The total simulation time was 1500 s. The main parameters of the simulated CPV plant are summarised in Table 1.

**Table 1.** Parameters of the concentration photovoltaic (CPV) plant simulated in PSCAD/EMTDC.

<b>CPV Trackers</b>	
Number of trackers: $n = 10$	
Maximum output power per tracker: 25 kW	
<b>HESS</b>	
<i>Batteries</i>	
12 batteries in series	Rated voltage: 12 V; capacity: 100 Ah
Inductance of the connection filter: $L_b = 1 \text{ mH}$	Resistance of the connection filter: $R_b = 100 \text{ m}\Omega$
<i>Ultracapacitors</i>	
Capacitance: $C_{uc} = 47 \text{ F}$	Rated voltage: 200 V
Inductance of the connection filter: $L_{uc} = 1 \text{ mH}$	Resistance of the connection filter: $R_{uc} = 100 \text{ m}\Omega$
<b>Distribution Grid</b>	
Root mean square (RMS) line-to-line voltage: 13.8 kV	Frequency: 50 Hz
<b>Grid Connection Transformer</b>	
Rated complex power: $S = 250 \text{ kVA}$	
Rated voltage windings: $U_{n1}/U_{n2} = 400 \text{ V}/13.8 \text{ kV}$	Star/delta connection
<b>Grid Connection Filter</b>	
Resistance: $R_g = 200 \text{ m}\Omega$	Inductance: $L_g = 2 \text{ mH}$
<b>DC-Link</b>	
Capacitor: $C_{bus} = 1360 \text{ }\mu\text{F}$	Reference for the DC-link voltage: 750 V
<b>Grid Converter</b>	
Two-Level VSC	Switching frequency: 10 kHz
<b>Converters of Batteries and Ultracapacitors</b>	
One-leg bidirectional DC–DC converters	Switching frequency: 10 kHz

All the control systems have been designed using the root-locus technique according to the desired poles of the different closed-loop systems. Although there are several design criteria, the poles of the closed-loop systems have been chosen as real values in order to avoid underdamped time responses [37], and they have been placed at the following locations:

- Control system of the active power injected into the grid (Figure 7). The pole is placed at  $s = -2$  rad/s.
- Control scheme of the DC–DC converters associated with the batteries and the ultracapacitors (Figure 10a,b). The poles of the resulting closed-loop system are located at  $s_1 = s_2 = -1000$  rad/s in both control systems.
- Control scheme of the  $d - q$  components of the current injected into the grid (Figure 11). The poles are located at  $s_1 = s_2 = -1000$  rad/s.
- Control scheme of the voltage of the DC-link (Figure 11). In this case, the resulting time response of the closed-loop system must be slower than the response of the inner control loop, that is, the control of the current injected into the grid. The chosen poles are, therefore, placed at  $s_1 = -100$  rad/s and  $s_2 = -20$  rad/s.

Furthermore, the transfer function of the filter  $H_{st}$  employed in Figure 8 is

$$H_{st} = \left( \frac{0.16}{s^2 + 0.8s + 0.16} \right)^3 \quad (26)$$

which is the same as the transfer function used in Figure 9.

All the CPV generators have been modelled as current sources with limited output voltage and power, as described in Section 2.1. Table 2 shows different values of the current generated for each CPV generator, which have been simulated over time to emulate various levels of solar radiation, including the case of clouds passing over the CPV plant, which implies that zero current is generated. These values are very similar, as it is assumed that all 10 CPV generators of the PV plant are identical, and slight differences are, therefore, justified with the same amount of solar radiation.

**Table 2.** Current generated by the concentration photovoltaic (CPV) panels throughout the time of the simulation.

Time Interval (s)	Current Generated by the CPV Panels (A)									
	$I_{pv1}$	$I_{pv2}$	$I_{pv3}$	$I_{pv4}$	$I_{pv5}$	$I_{pv6}$	$I_{pv7}$	$I_{pv8}$	$I_{pv9}$	$I_{pv10}$
$0 \leq t \leq 1$	0	0	0	0	0	0	0	0	0	0
$1 \leq t \leq 400$	20	19	20.5	18	20	19	20	21.5	22	20
$400 \leq t \leq 800$	33	32	33.5	31	33	33	31	33.5	34	33
$800 \leq t \leq 900$	0	0	0	0	0	0	0	0	0	0
$900 \leq t \leq 1200$	15	14.5	16	15	15	17	16	15.5	16	15
$1200 \leq t \leq 1500$	25	24	26	26	25	26	24	26	27	25

Because the voltage of the DC-link is controlled in order to maintain a value of 750 V (as detailed in Table 1), the power generated by each CPV panel can be obtained by multiplying its respective generated current by the DC-link voltage. These powers are shown in Table 3 and in Figure 12: the values of the powers generated change greatly as a consequence of the changes in solar radiation. The time interval  $800 \text{ s} \leq t \leq 900 \text{ s}$  is particularly noteworthy, as the power generated by all the trackers is zero owing to the fact that, for example, several clouds can block direct solar radiation.

**Table 3.** Power generated by the concentration photovoltaic (CPV) panels over time, assuming a DC-link voltage of 750 V.

Time Interval (s)	Power Generated by the CPV Panels (kW)									
	$P_{pv1}$	$P_{pv2}$	$P_{pv3}$	$P_{pv4}$	$P_{pv5}$	$P_{pv6}$	$P_{pv7}$	$P_{pv8}$	$P_{pv9}$	$P_{pv10}$
$0 \leq t \leq 1$	0	0	0	0	0	0	0	0	0	0
$1 \leq t \leq 400$	15	14.25	15.38	13.5	15	14.25	15	16.13	16.5	15
$400 \leq t \leq 800$	24.75	24	25.13	23.25	24.75	24.75	23.25	25.13	25.5	24.75
$800 \leq t \leq 900$	0	0	0	0	0	0	0	0	0	0
$900 \leq t \leq 1200$	11.25	10.88	12	11.25	11.25	12.75	12	11.63	12	11.25
$1200 \leq t \leq 1500$	18.75	18	19.5	19.5	18.75	19.5	18	19.5	20.25	18.75

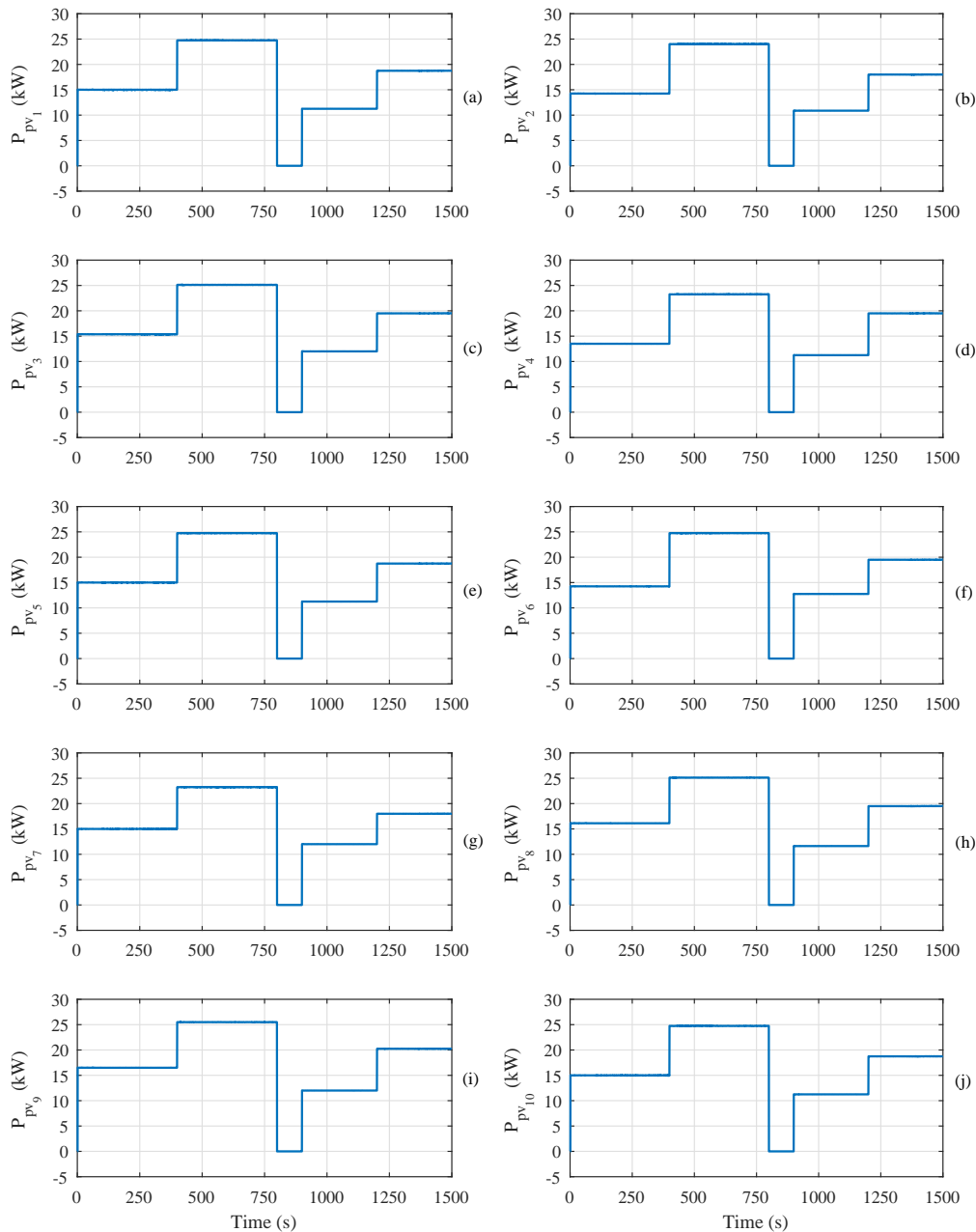


**Figure 12.** Time responses of the power generated by the 10 concentration photovoltaic (CPV) generators of the PV plant. (a)  $p_{pv1}$ ; (b)  $p_{pv2}$ ; (c)  $p_{pv3}$ ; (d)  $p_{pv4}$ ; (e)  $p_{pv5}$ ; (f)  $p_{pv6}$ ; (g)  $p_{pv7}$ ; (h)  $p_{pv8}$ ; (i)  $p_{pv9}$ ; and (j)  $p_{pv10}$ .

Figure 13 shows the active powers generated by the 10 trackers and their associated HESS of the CPV plant: in accordance with the control scheme depicted in Figure 7, each tracker–HESS set generates 20 kW in steady state, which is equal to the reference value of the active power, that is,  $p_g^* = 20$  kW. The control scheme plotted in Figure 7 is, therefore, able to attain zero tracking error for constant set-points, as demonstrated in Equation (15). Furthermore, small transients occur when the active powers generated by all the trackers are zero in the time interval  $800 \text{ s} \leq t \leq 900 \text{ s}$  and are quickly compensated for by the control system, as shown in Figure 7.

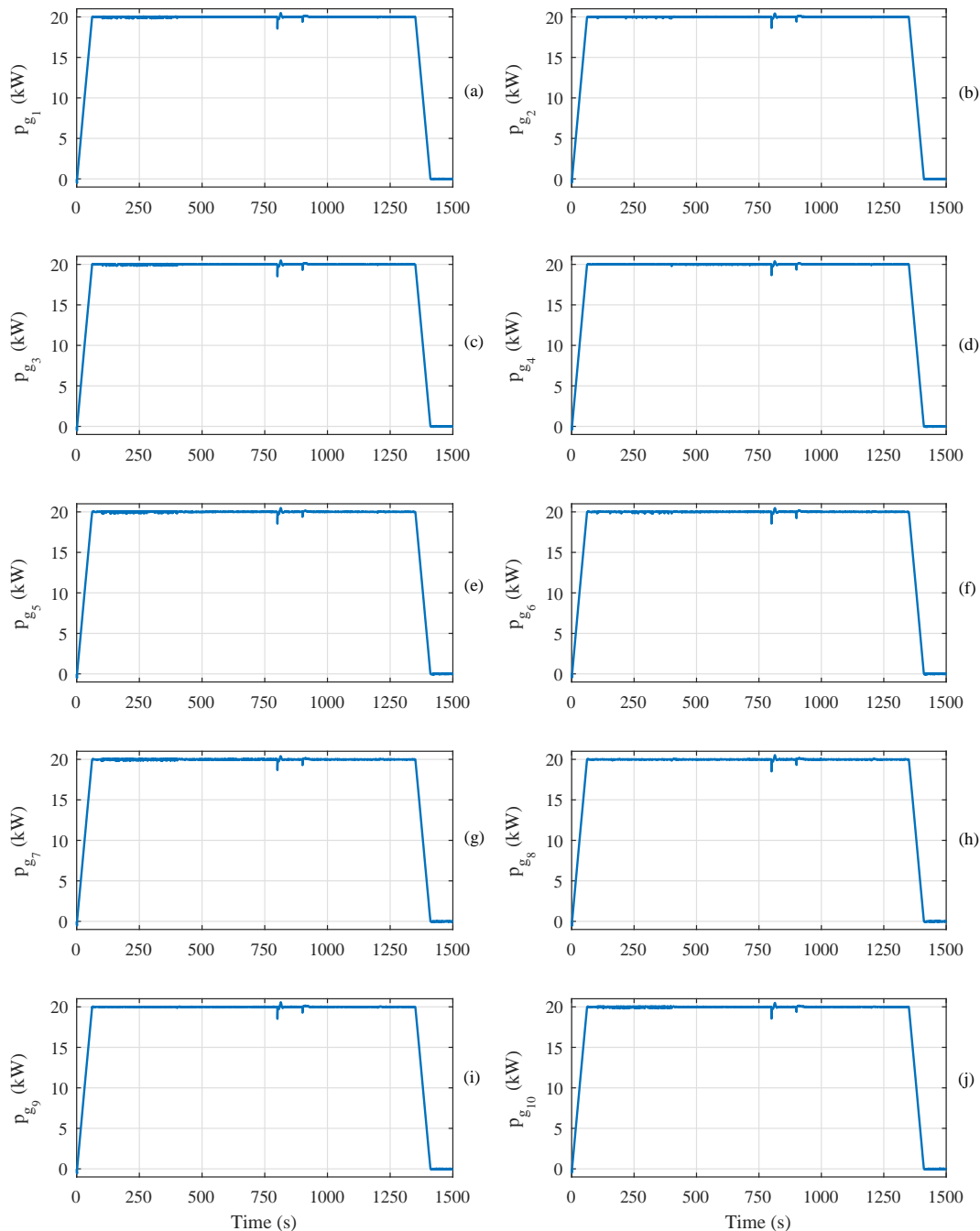


**Figure 13.** Individual time responses of the power generated by the 10 tracker–hybrid energy storage system (HESS) units. (a)  $p_{g_1}$ ; (b)  $p_{g_2}$ ; (c)  $p_{g_3}$ ; (d)  $p_{g_4}$ ; (e)  $p_{g_5}$ ; (f)  $p_{g_6}$ ; (g)  $p_{g_7}$ ; (h)  $p_{g_8}$ ; (i)  $p_{g_9}$ ; and (j)  $p_{g_{10}}$ .

The total active power injected into the grid by the CPV plant is shown in Figure 14: the steady-state value is 200 kW, which is the sum of all the individual contributions of the active

powers generated by the 10 tracker–HESS units plotted in Figure 13. Moreover, the total reactive power injected into the grid by the CPV plant is plotted in Figure 15: the value injected is around 50 kVAr, and both the active and the reactive powers are completely decoupled, as shown in Figures 14 and 15.

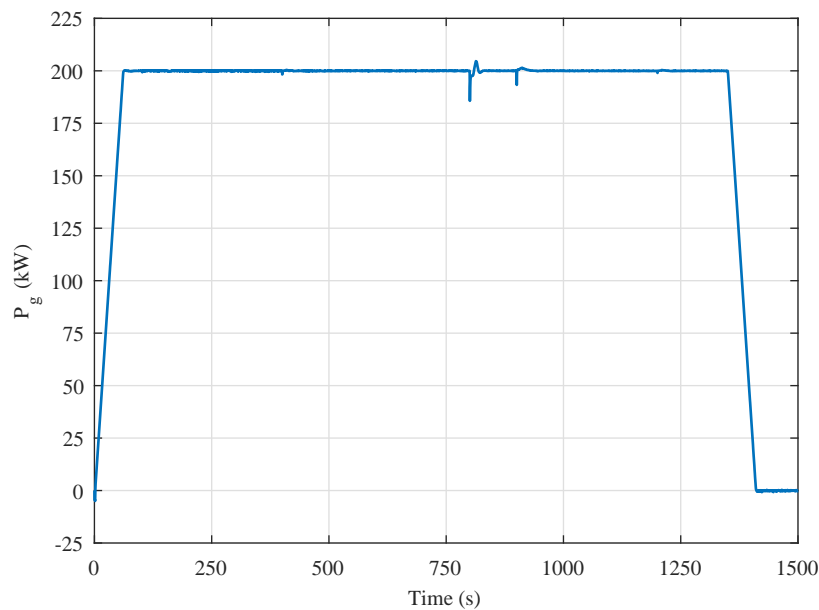


**Figure 14.** Time response of the total active power injected into the grid by the concentration photovoltaic (CPV) plant.

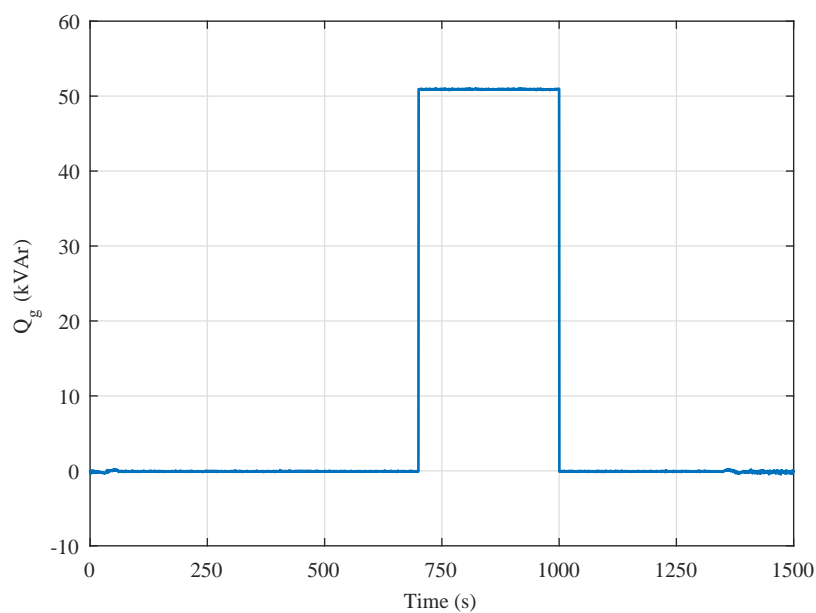


**Figure 15.** Time response of the total reactive power injected into the grid by the concentration photovoltaic (CPV) plant.

The results plotted in Figures 13 and 14 show that the power injected into the grid has a smooth profile owing to the use of the HESS: Figure 16 shows how the 10 HESSs are able to absorb the high variations of the powers generated by the 10 CPV trackers, as plotted in Figure 12, in order to obtain the grid-power profile shown in Figure 14. These results also show that the control system depicted in Figure 7 performs effectively.

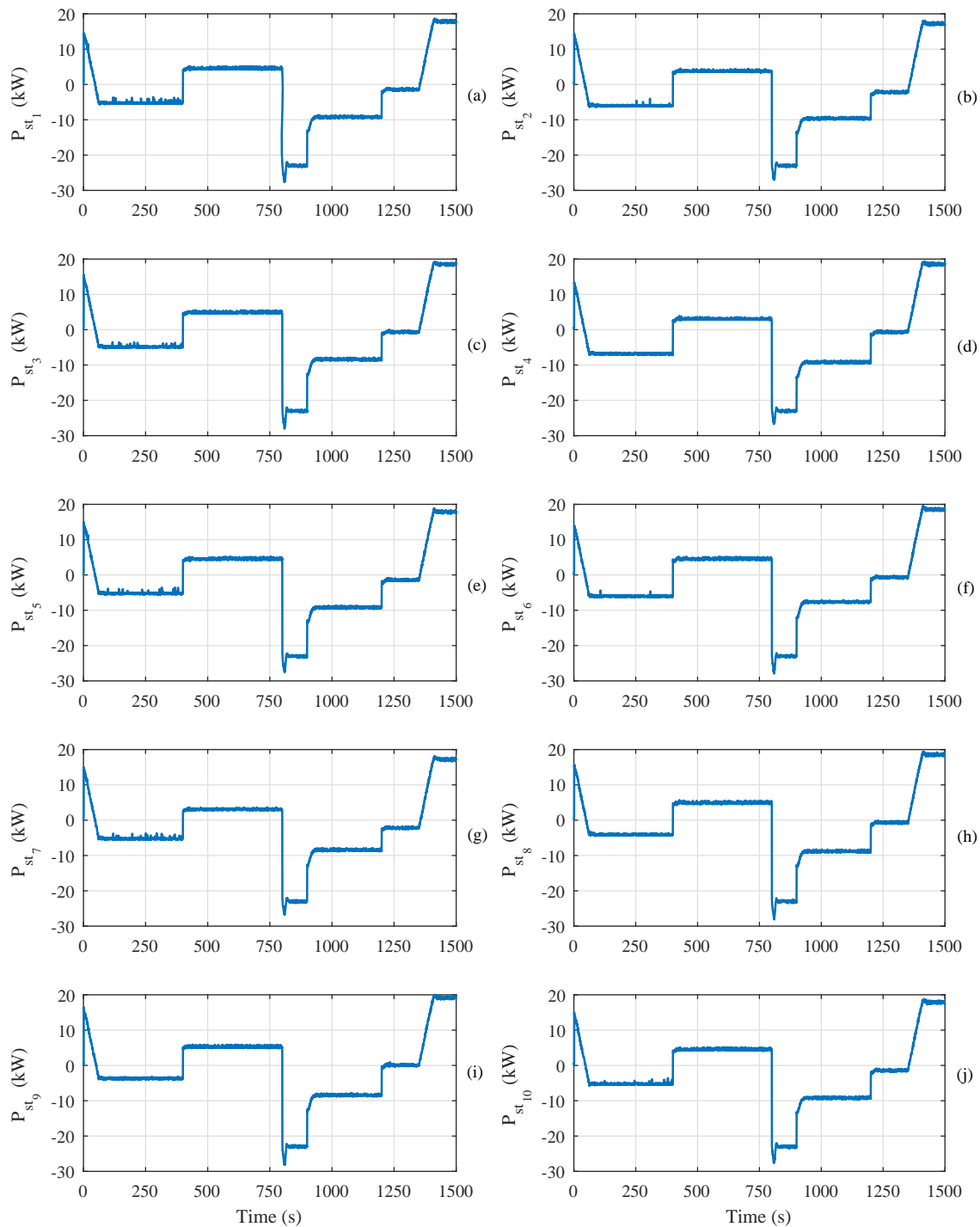


**Figure 16.** Time responses of the power exchanged by the 10 hybrid energy storage systems (HESs).

(a)  $p_{st_1}$ ; (b)  $p_{st_2}$ ; (c)  $p_{st_3}$ ; (d)  $p_{st_4}$ ; (e)  $p_{st_5}$ ; (f)  $p_{st_6}$ ; (g)  $p_{st_7}$ ; (h)  $p_{st_8}$ ; (i)  $p_{st_9}$ ; and (j)  $p_{st_{10}}$ .

Figure 17 shows the power generated or absorbed by the ultracapacitors, whereas the power generated or absorbed by the banks of batteries is plotted in Figure 18. According to the transfer function of the filter  $H_{st}$  in Equation (26) and the scheme shown in Figure 8, the time responses of the ultracapacitor powers have rapid variations, including transients, which implies high-frequency components, while the power profile of the batteries contains low-frequency components, with slow variations in the power.

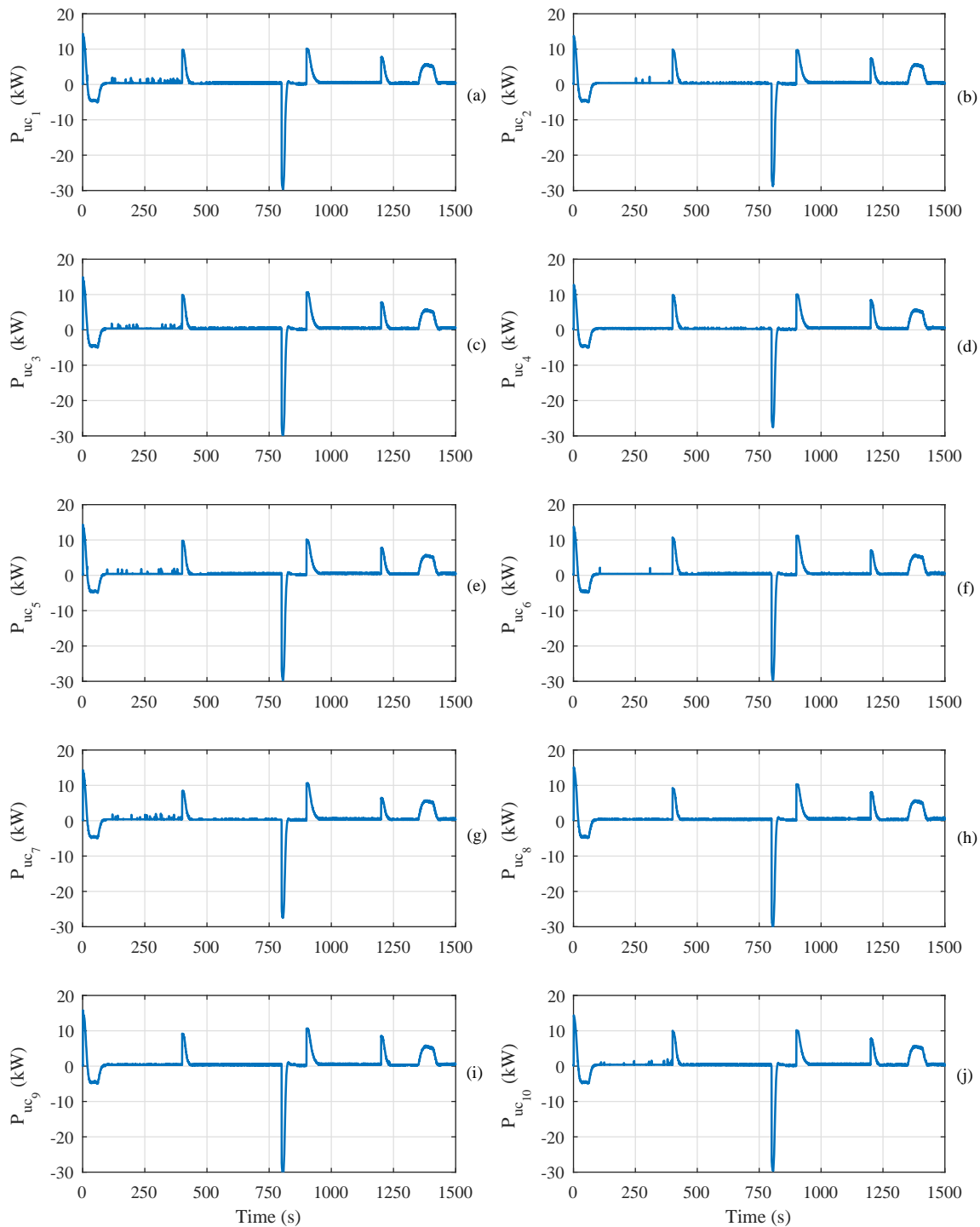


**Figure 17.** Powers generated/absorbed by the ultracapacitors of the 10 hybrid energy storage systems (HESSs). (a)  $p_{uc_1}$ ; (b)  $p_{uc_2}$ ; (c)  $p_{uc_3}$ ; (d)  $p_{uc_4}$ ; (e)  $p_{uc_5}$ ; (f)  $p_{uc_6}$ ; (g)  $p_{uc_7}$ ; (h)  $p_{uc_8}$ ; (i)  $p_{uc_9}$ ; and (j)  $p_{uc_{10}}$ .

The currents through the ultracapacitors are plotted in Figure 19, while the voltages of the ultracapacitors are shown in Figure 20. The control of the currents through the ultracapacitors is implemented using the control scheme shown in Figure 10b. The ultracapacitors are able to provide high-peak currents in short periods of time in order to accomplish the power-profile requirements. When the currents are negative, the voltages of the ultracapacitors decrease as they are delivering energy, whereas when the currents are positive, the voltages increase, as the ultracapacitors store energy. It should be noted that the currents through the ultracapacitors and also the powers are zero

in steady state (see Figures 17 and 19). Furthermore, the discharge level of the ultracapacitors can be even higher than 50% with regard to the initial voltage value, that is, 150 V, as shown in Figure 20.

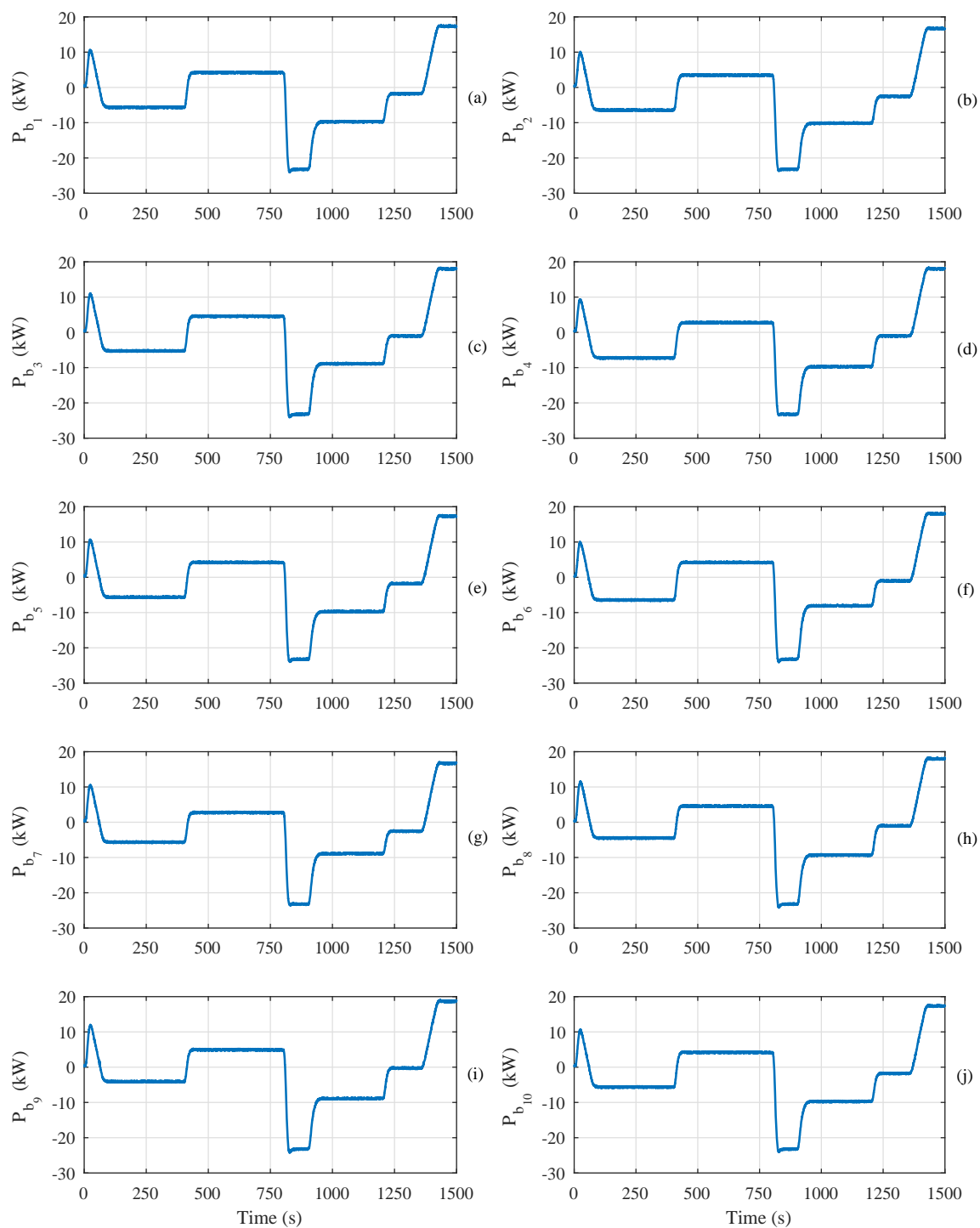


**Figure 18.** Powers generated/absorbed by the banks of batteries of the 10 hybrid energy storage systems (HESs). (a)  $p_{b_1}$ ; (b)  $p_{b_2}$ ; (c)  $p_{b_3}$ ; (d)  $p_{b_4}$ ; (e)  $p_{b_5}$ ; (f)  $p_{b_6}$ ; (g)  $p_{b_7}$ ; (h)  $p_{b_8}$ ; (i)  $p_{b_9}$ ; and (j)  $p_{b_{10}}$ .

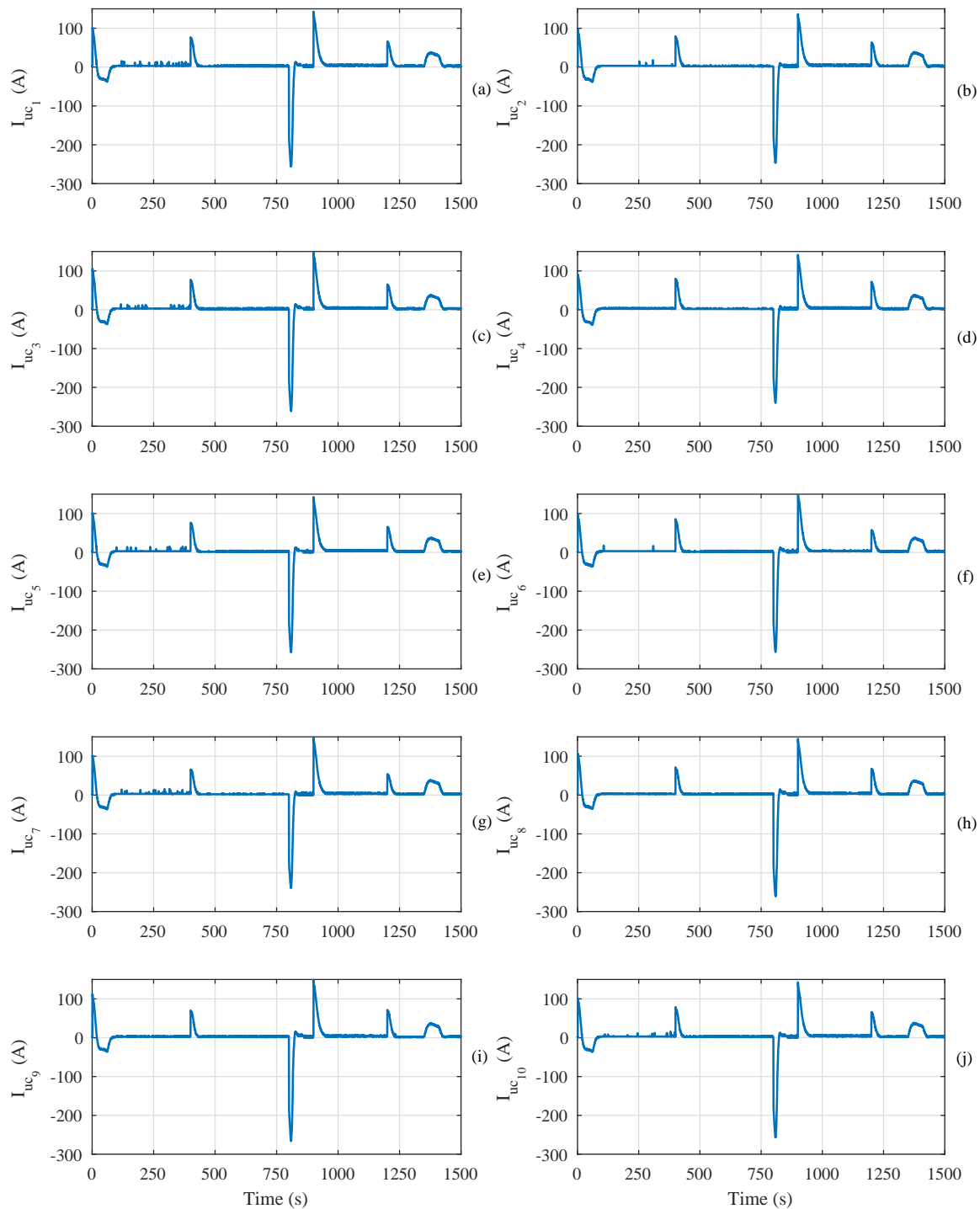


**Figure 19.** Currents through the ultracapacitors of the 10 hybrid energy storage systems (HESs). (a)  $i_{UC_1}$ ; (b)  $i_{UC_2}$ ; (c)  $i_{UC_3}$ ; (d)  $i_{UC_4}$ ; (e)  $i_{UC_5}$ ; (f)  $i_{UC_6}$ ; (g)  $i_{UC_7}$ ; (h)  $i_{UC_8}$ ; (i)  $i_{UC_9}$ ; and (j)  $i_{UC_{10}}$ .

Similar results can be seen in Figures 21 and 22, in which the current through the battery banks and the voltages of the batteries banks, respectively, are plotted; in this case the currents are calculated according to the control configuration depicted in Figure 10a, and their peak values are smaller than in the case of the ultracapacitors. Moreover, slower variations take place. Once the steady state of the time response of the filter  $H_{st}$  has been attained and the currents provided by the ultracapacitors are zero, the batteries provide all the current required by the storage system. Furthermore, as the energy density of the batteries is higher than that of the ultracapacitors, the discharge levels of the

batteries are greatly reduced in the simulation period when compared to those of the ultracapacitors (see Figures 20 and 22 to observe the differences).

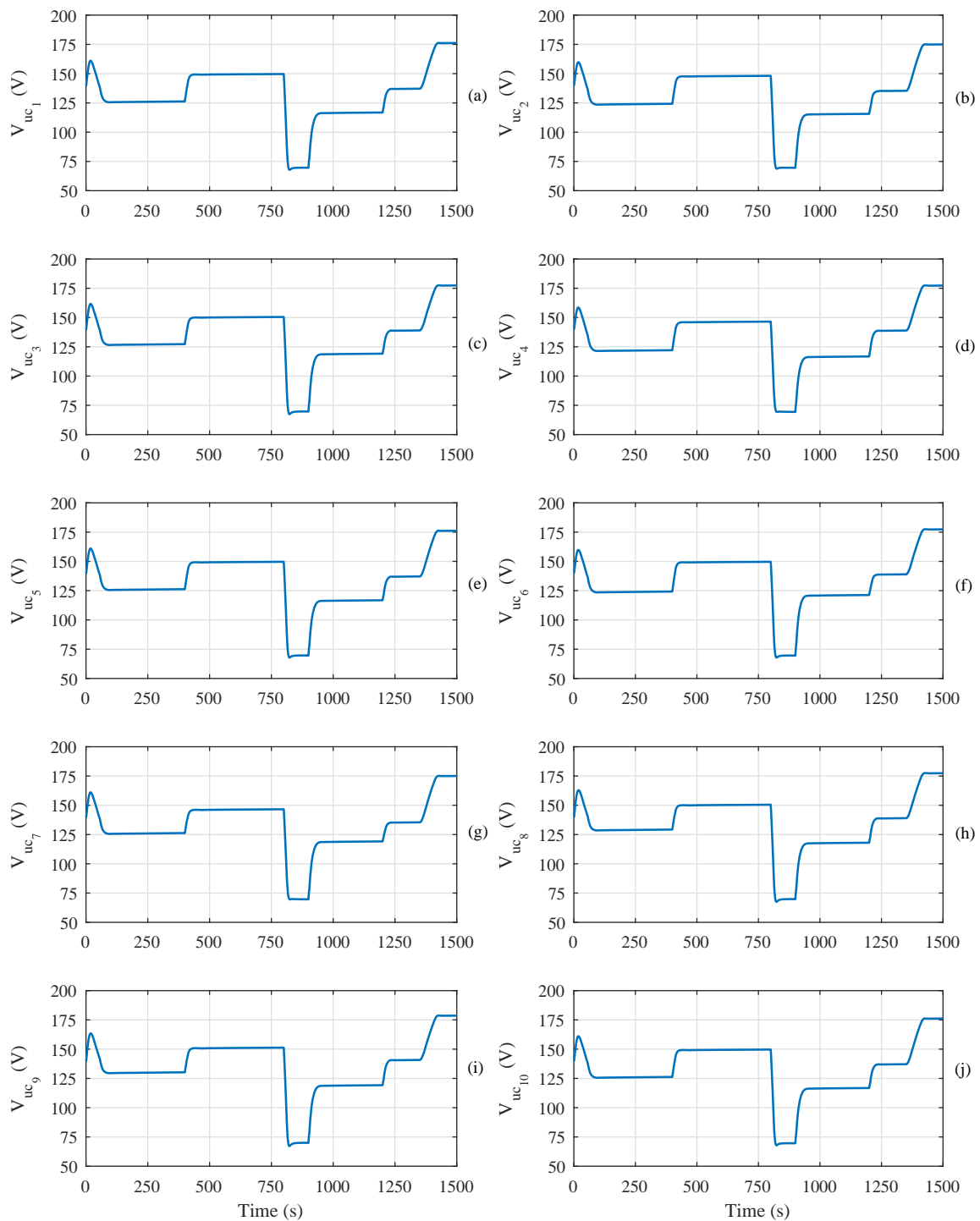


**Figure 20.** Voltages of the ultracapacitors of the 10 hybrid energy storage systems (HESs). (a)  $v_{uc_1}$ ; (b)  $v_{uc_2}$ ; (c)  $v_{uc_3}$ ; (d)  $v_{uc_4}$ ; (e)  $v_{uc_5}$ ; (f)  $v_{uc_6}$ ; (g)  $v_{uc_7}$ ; (h)  $v_{uc_8}$ ; (i)  $v_{uc_9}$ ; and (j)  $v_{uc_{10}}$ .

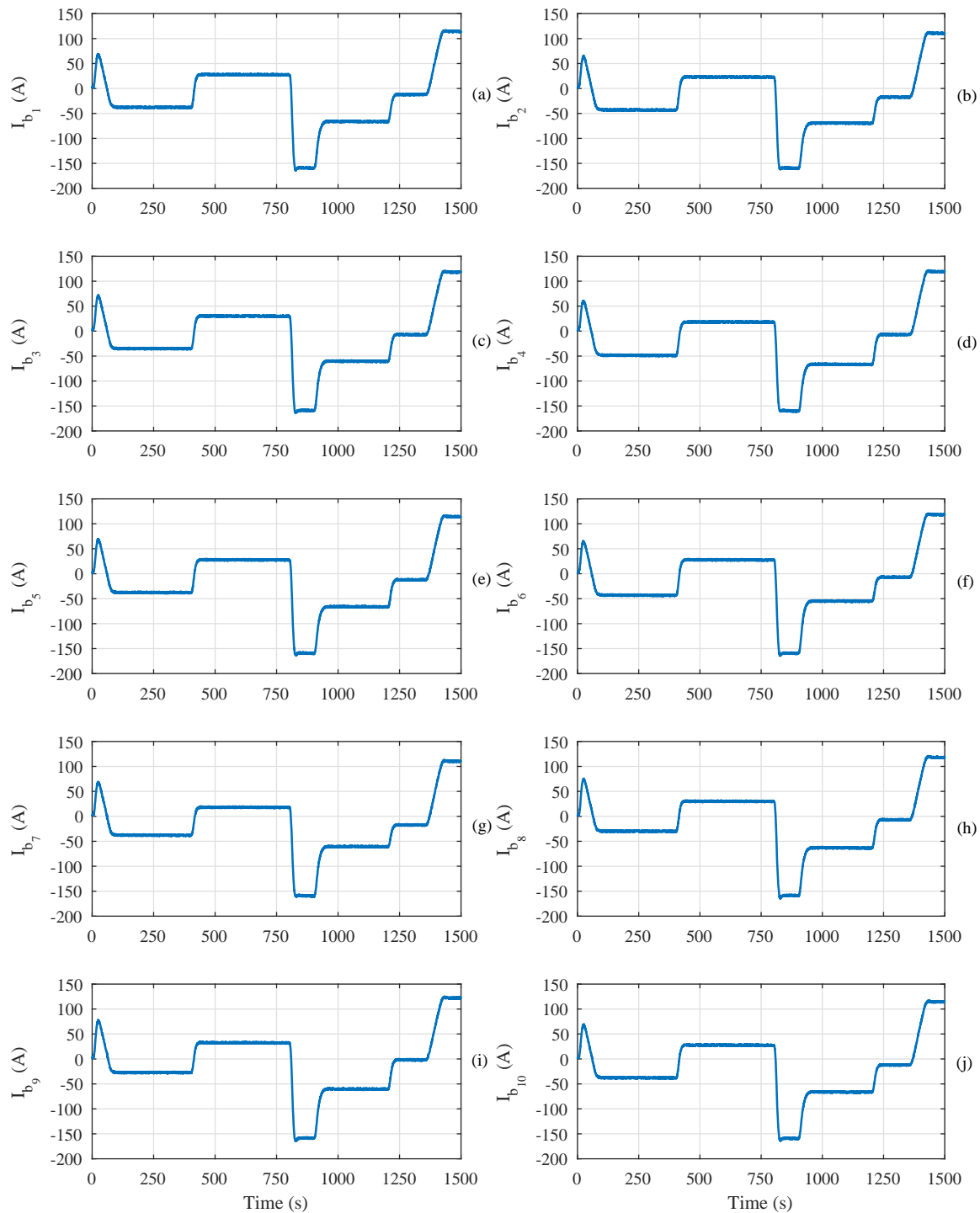


**Figure 21.** Currents through the banks of batteries of the 10 hybrid energy storage systems (HESs). (a)  $i_{b_1}$ ; (b)  $i_{b_2}$ ; (c)  $i_{b_3}$ ; (d)  $i_{b_4}$ ; (e)  $i_{b_5}$ ; (f)  $i_{b_6}$ ; (g)  $i_{b_7}$ ; (h)  $i_{b_8}$ ; (i)  $i_{b_9}$ ; and (j)  $i_{b_{10}}$ .

### Performance of the Control System

Previous results show that the control system deals with the variations of the powers generated by the CPV panels throughout time in order to maintain a constant power profile injected into the grid. The simulations are mainly focused on the steady-state response; however the transient response must be analysed.

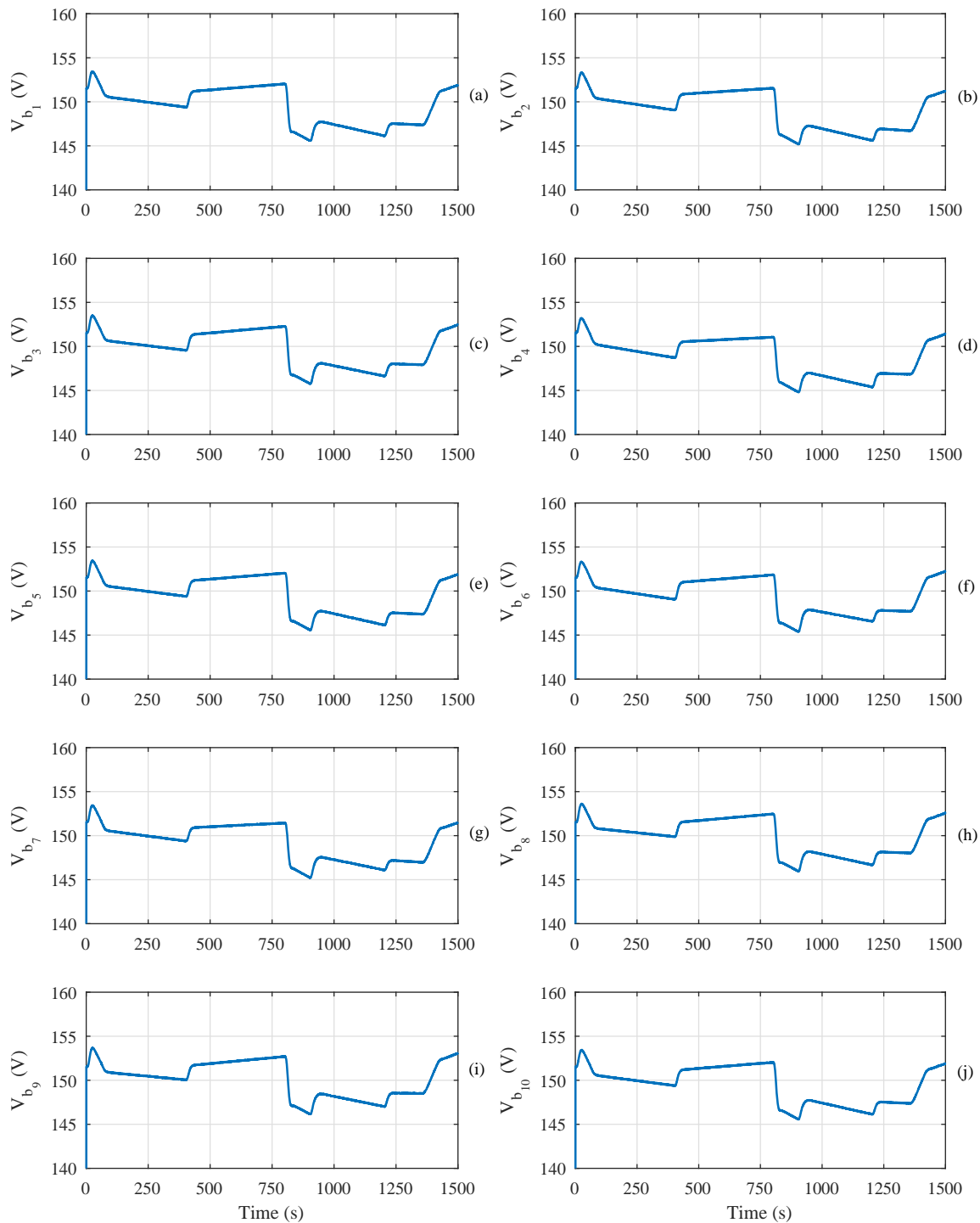


**Figure 22.** Voltages of the banks of batteries the 10 hybrid energy storage systems (HESSs). (a)  $v_{b_1}$ ; (b)  $v_{b_2}$ ; (c)  $v_{b_3}$ ; (d)  $v_{b_4}$ ; (e)  $v_{b_5}$ ; (f)  $v_{b_6}$ ; (g)  $v_{b_7}$ ; (h)  $v_{b_8}$ ; (i)  $v_{b_9}$ ; and (j)  $v_{b_{10}}$ .

This section presents the dynamic performances of the designed control schemes. For this purpose, the time instant  $t = 400$  s has been chosen, as it is one of the instants in which the powers generated by the CPV panels change their values.

Although the results obtained for the 10 CPV generators are different, Figures 16–22 show that the previous simulation results are similar. For this reason, only the dynamic performances of the control schemes of the tracker  $CPV_1$  have been analysed.

Figure 23 shows the results obtained with the control system depicted in Figure 7: at the instant  $t = 400$  s, the power generated by the CPV panels,  $p_{cpv}$ , changes from 15 to 24.75 kW, as shown in Figure 23a. The control system keeps the value of the power injected into the grid at the reference value, that is, 20 kW, in steady state, as shown in Figure 23b,c. In accordance with Equation (12), the power of the DC-link capacitor changes its value with the variations of the power  $p_{cpv}$ , which means that the power  $p_g$  also varies, as  $p_{C_{bus}}$  is a disturbance in the control scheme shown in Figure 7. The regulator  $R_{p_g}(s)$  changes the value of  $p_g$  to the reference value with a transient response of 2 s, approximately, by modifying the reference value of the HESS power,  $p_{st}^*$  (as can be seen in Figure 23d for the time interval  $400 \text{ s} < t < 402 \text{ s}$ ). Furthermore, Figure 23d,e shows that  $p_{st}^*$  and  $p_{st}$  are almost identical, which means that the dynamics of the ESS can be neglected and can be approximated by unity.

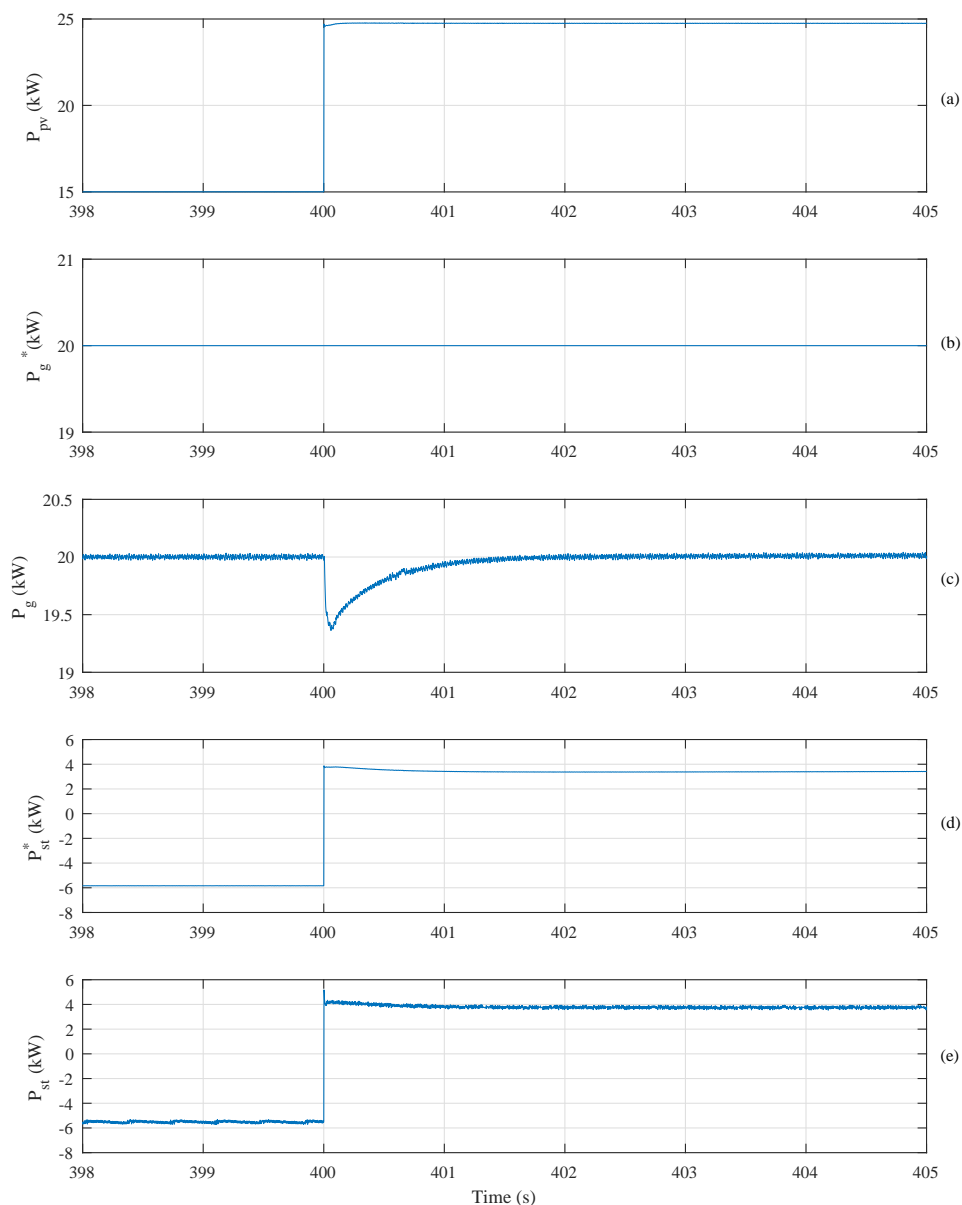


**Figure 23.** Results obtained for  $CPV_1$ . Time responses of (a) power generated by the concentration photovoltaic (CPV) panel,  $p_{pv}$ ; (b) reference of the grid power,  $p_g^*$ ; (c) power injected into the grid,  $p_g$ ; (d) reference of the hybrid energy storage system (HESS) power,  $p_{st}^*$ ; and (e) power of the HESS,  $p_{st}$ .

Figure 24 shows the behaviour of the control systems of the DC–DC converters associated to the batteries and the ultracapacitors (depicted in Figure 10a,b, respectively). A larger time interval than

that plotted in Figure 23 has been defined in order to show the dynamics of the filter  $H_{st}(s)$ . Figure 24a shows that the current reference of the batteries varies slowly. However, the value of the current reference of the ultracapacitors changes suddenly (as shown in Figure 24d), in accordance with the scheme proposed in Figure 8. Because the current controllers are designed in order to obtain closed-loop poles located at  $s_1 = s_2 = -1000$  rad/s, the currents of the batteries are practically equal to its reference in the time interval employed (see Figure 24a,b). The same conclusion is obtained when analysing the currents of the ultracapacitors and their reference value, as shown in Figure 24d,e. Figure 24c shows the reference voltage for the DC–DC converter associated to the batteries; this reference voltage is very similar to the voltage of the battery in steady state, which can be seen in Figure 22a. Moreover, the reference voltage for the DC–DC converter associated to the ultracapacitor is equal to the voltage of the ultracapacitor in steady state, as shown in Figures 20a and 24f, because the current of the ultracapacitors is zero in steady state.

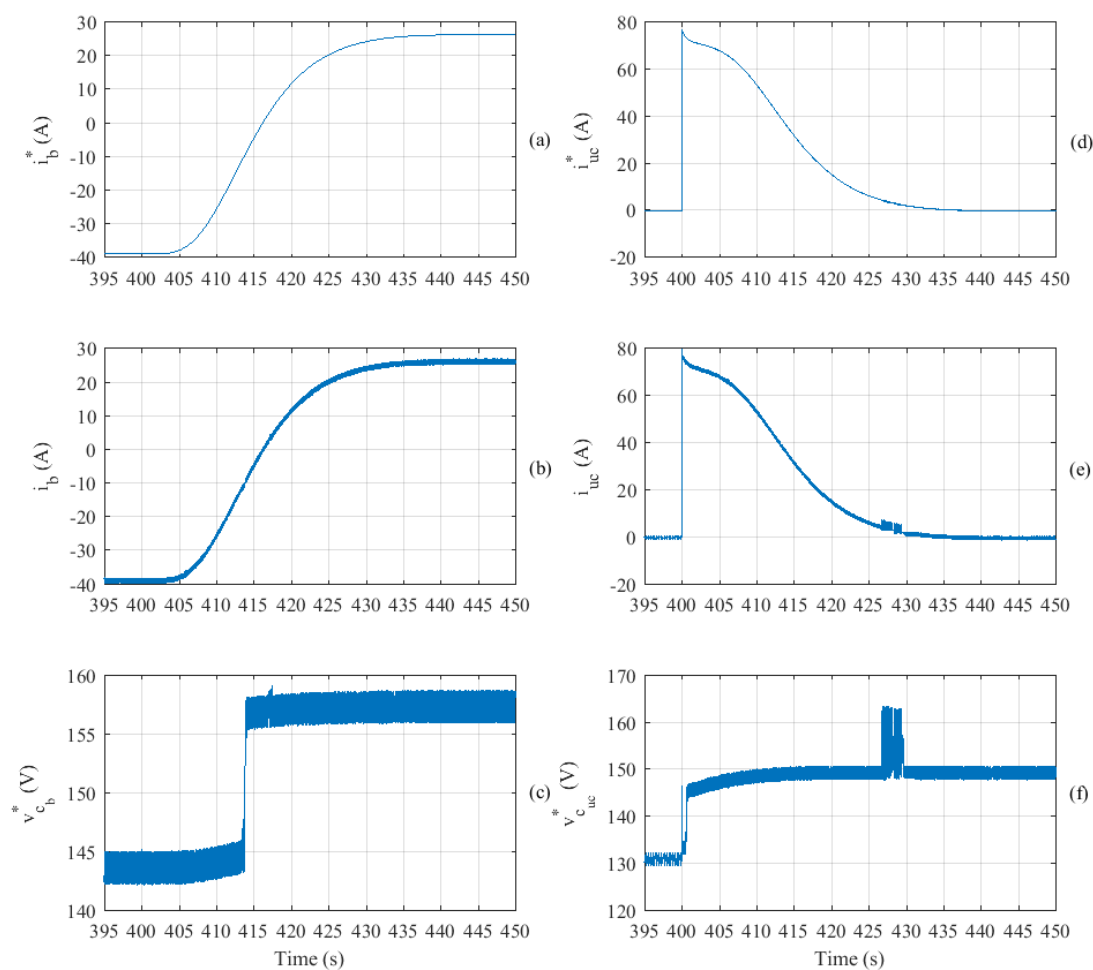


**Figure 24.** Results obtained for  $CPV_1$ . Time responses of (a) reference of the battery current,  $i_b^*$ ; (b) current of the batteries,  $i_b$ ; (c) reference voltage for the DC–DC converter associated to the bank of the batteries,  $v_{c_b}^*$ ; (d) reference of the ultracapacitor current,  $i_{uc}^*$ ; (e) current of the ultracapacitors,  $i_{uc}$ ; and (f) reference voltage for the DC–DC converter associated to the ultracapacitors,  $v_{c_{uc}}^*$ .

The dynamic performance of the control scheme of the DC-link voltage and the grid-connected converter, plotted in Figure 11, can be analysed in Figure 25; the reference voltage of the DC-link is always 750 V. Because the power  $p_{pv}$  changes at  $t = 400$  s, the voltage of the DC-link is also modified according to Equation (20), as Figure 25b shows. The regulator  $R_{v_{C_{bus}}}(s)$  changes the reference of the  $d$ -axis current,  $i_{gd}^*$ , in order to keep the true voltage equal to its reference, which is achieved at  $t = 401$  s,

approximately. The reference  $i_{gd}^*$  and the  $d$  component of the grid current  $i_{gd}$ , plotted in Figure 25c,d, respectively, are almost equal in the time interval used in Figure 25, as the parameters of the current controllers of the grid-connected converter have been designed using the same specifications as those of the control systems of the DC–DC converters associated to the batteries and the ultracapacitors. The reactive power reference is zero at  $t = 400$  s, which implies that both the reference,  $i_{gq}^*$ , and the  $q$  component of the grid current,  $i_{gq}$ , are zero, as shown in Figure 25e,f. Finally, Figure 25g,h shows the reference voltages  $u_d^*$  and  $u_q^*$ , respectively, for the grid-connected converter.

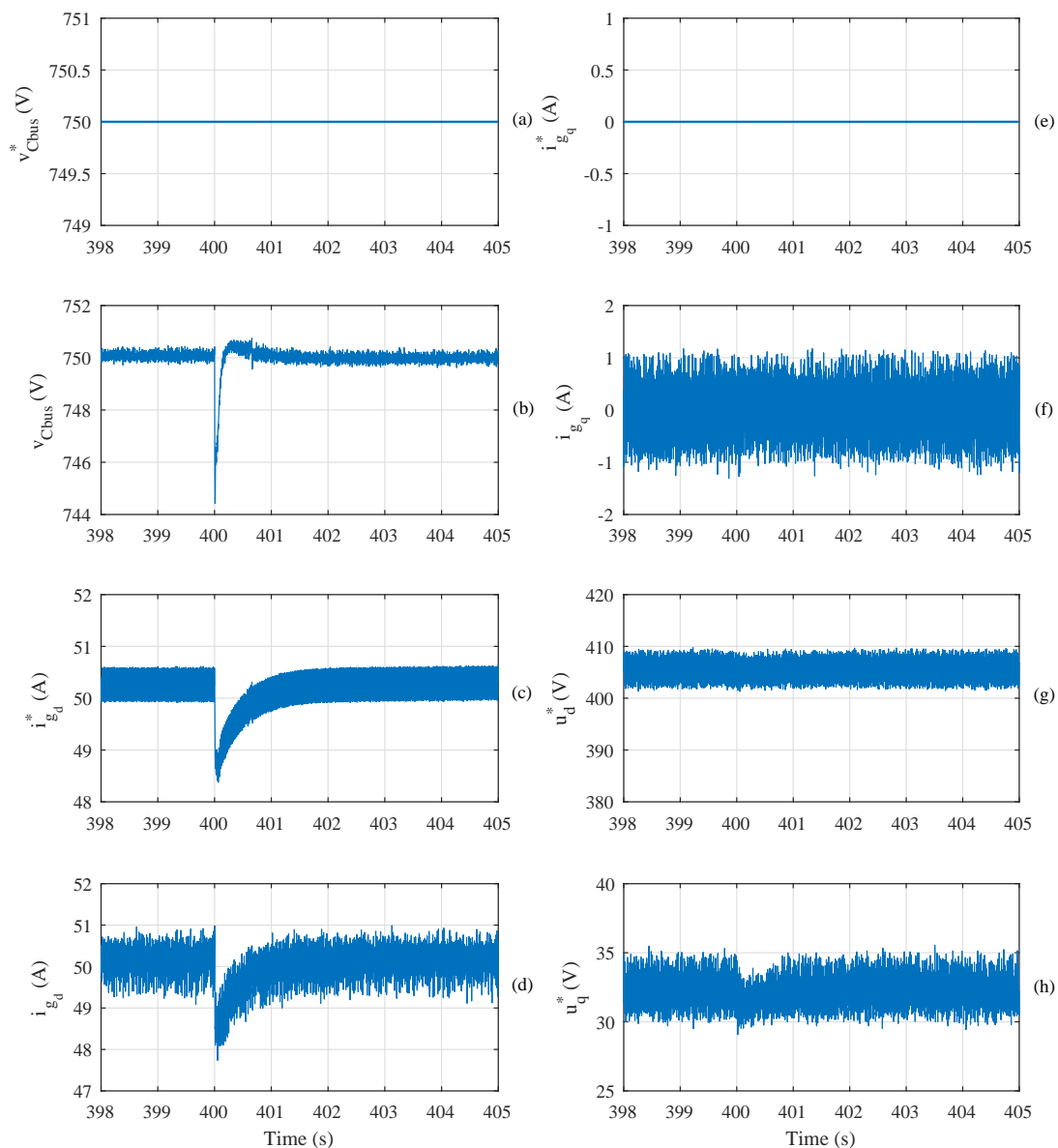


**Figure 25.** Results obtained for  $CPV_1$ . Time responses of (a) reference of the voltage of the DC-link,  $v_{Cbus}^*$ ; (b) voltage of the DC-link,  $v_{Cbus}$ ; (c) reference of the  $d$ -axis of the current,  $i_{gd}^*$ ; (d) current,  $i_{gd}$ ; (e) reference of the  $q$ -axis of the current,  $i_{gq}^*$ ; (f) current,  $i_{gq}$ ; (g)  $d$  component of the reference voltage of the converter,  $u_d^*$ ; and (h)  $q$  component of the reference voltage of the converter,  $u_q^*$ .

## 5. Conclusions

The combined use of ultracapacitors and batteries is a very effective solution by which to satisfy the short-term energy storage requirements demanded by CPV systems. In this paper, the design of the control system of a 200 kW CPV power plant connected to the grid with a HESS has been

presented. The integration of the different elements has been carried out by means of power electronic converters. The complete control system is split into various subsystems, namely, the control schemes of the batteries and the ultracapacitors, the controller of the voltage of the DC-link, and the controller for the grid-connected converter. Furthermore, an energy management system based on a closed-loop structure has been developed in order to inject a constant active power profile into the grid. Simulation results are provided by means of a case study implemented in PSCAD/EMTDC, which showed a very precise and independent control of the power flow in the different components. Furthermore, a decoupled control of the active and reactive powers injected into the grid has also been achieved. The overall performance of the CPV generation system is, therefore, enhanced by means of the integrated energy storage, thus providing an efficient solution that can easily be scaled.

**Acknowledgments:** This work has been supported by the Ministry of Economy and Competitiveness of Spain and by the European Regional Development Fund under the research project ENE2015-71417-R (MINECO/FEDER, UE).

**Author Contributions:** Pedro Roncero-Sánchez defined the control-system configuration. Alfonso Parreño Torres was responsible of the design of the case study, while the simulations were carried out by Javier Vázquez. All the authors have participated in the writing process of the paper.

**Conflicts of Interest:** The authors declare no conflict of interest. The founding sponsors had no role in the design of the study; in the collection, analyses, or interpretation of data; in the writing of the manuscript; or in the decision to publish the results.

## References

1. Akinyele, D.; Rayudu, R. Review of energy storage technologies for sustainable power networks. *Sustain. Energy Technol. Assess.* **2014**, *8*, 74–91.
2. Singh, M.; Khadkikar, V.; Chandra, A.; Varma, R.K. Grid Interconnection of Renewable Energy Sources at the Distribution Level with Power-Quality Improvement Features. *IEEE Trans. Power Deliv.* **2011**, *26*, 307–315.
3. Beltran, H.; Bilbao, E.; Belenguer, E.; Etxeberria-Otadui, I.; Rodriguez, P. Evaluation of Storage Energy Requirements for Constant Production in PV Power Plants. *IEEE Trans. Ind. Electron.* **2013**, *60*, 1225–1234.
4. Barton, J.P.; Infield, D.G. Energy storage and its use with intermittent renewable energy. *IEEE Trans. Energy Convers.* **2004**, *19*, 441–448.
5. Gabash, A.; Li, P. Active-Reactive Optimal Power Flow in Distribution Networks with Embedded Generation and Battery Storage. *IEEE Trans. Power Syst.* **2012**, *27*, 2026–2035.
6. Roncero-Sánchez, P.; Roncero-Clemente, C.; Romero-Cadaval, E.; Husev, O.; Makovenko, E. Control scheme of a Three-Phase Three-Level NPC qZ-Source inverter with LCL filter for RES applications. In Proceedings of the 42nd Annual Conference of the IEEE Industrial Electronics Society, IECON 2016, Florence, Italy, 23–26 October 2016; pp. 6540–6547.
7. Dimroth, F.; Philipps, S.P.; Peharz, G.; Welsler, E.; Kellenbenz, R.; Roesener, T.; Klingner, V.; Oliva, E.; Steiner, M.; Meusel, M.; et al. Promises of advanced multi-junction solar cells for the use in CPV systems. In Proceedings of the 35th IEEE Photovoltaic Specialists Conference, Honolulu, HI, USA, 20–25 June 2010; pp. 1231–1236.
8. Elerath, J.G. HCPV tracker accelerated reliability tests. In Proceedings of the 35th IEEE Photovoltaic Specialists Conference, Honolulu, HI, USA, 20–25 June 2010; pp. 481–486.
9. Furman, B.; Menard, E.; Gray, A.; Meitl, M.; Bonafede, S.; Kneeburg, D.; Ghosal, K.; Bukovnik, R.; Wagner, W.; Gabriel, J.; et al. A high concentration photovoltaic module utilizing micro-transfer printing and surface mount technology. In Proceedings of the 35th IEEE Photovoltaic Specialists Conference, Honolulu, HI, USA, 20–25 June 2010; pp. 475–480.
10. Haney, M.W.; Gu, T.; Agrawal, G. Hybrid micro-scale CPV/PV architecture. In Proceedings of the 40th IEEE Photovoltaic Specialists Conference, Denver, CO, USA, 8–13 June 2014; pp. 2122–2126.
11. Castillo, A.; Gayme, D.F. Grid-scale energy storage applications in renewable energy integration: A survey. *Energy Convers. Manag.* **2014**, *87*, 885–894.
12. Zhou, H.; Bhattacharya, T.; Tran, D.; Siew, T.S.T.; Khambadkone, A.M. Composite Energy Storage System Involving Battery and Ultracapacitor with Dynamic Energy Management in Microgrid Applications. *IEEE Trans. Ind. Electron.* **2011**, *26*, 923–930.

13. Suberu, M.Y.; Mustafa, M.W.; Bashir, N. Energy storage systems for renewable energy power sector integration and mitigation of intermittency. *Renew. Sustain. Energy Rev.* **2014**, *35*, 499–514.
14. Vazquez, S.; Lukic, S.M.; Galvan, E.; Franquelo, L.G.; Carrasco, J.M. Energy Storage Systems for Transport and Grid Applications. *IEEE Trans. Ind. Electron.* **2010**, *57*, 3881–3895.
15. Gharibeh, H.F.; Yazdankhah, A.S.; Azizian, M.R. Improved energy management for a power-split multi-source fuel cell vehicle based on optimal source sizing and regenerative braking. In Proceedings of the 16th IEEE International Conference on Environment and Electrical Engineering (EEEIC2016), Florence, Italy, 7–10 June 2016; pp. 1–6.
16. Momayyezani, M.; Abeywardana, D.B.W.; Hredzak, B.; Agelidis, V.G. Integrated Reconfigurable Configuration for Battery/Ultracapacitor Hybrid Energy Storage Systems. *IEEE Trans. Energy Convers.* **2016**, *31*, 1583–1590.
17. Cao, J.; Emadi, A. A New Battery/UltraCapacitor Hybrid Energy Storage System for Electric, Hybrid, and Plug-In Hybrid Electric Vehicles. *IEEE Trans. Power Electron.* **2012**, *27*, 122–132.
18. Camara, M.B.; Gualous, H.; Gustin, F.; Berthon, A. Design and New Control of DC/DC Converters to Share Energy between Supercapacitors and Batteries in Hybrid Vehicles. *IEEE Trans. Veh. Technol.* **2008**, *57*, 2721–2735.
19. Song, Z.; Hofmann, H.; Li, J.; Hou, J.; Han, X.; Ouyang, M. Energy management strategies comparison for electric vehicles with hybrid energy storage system. *Appl. Energy* **2014**, *134*, 321–331.
20. Song, Z.; Hou, J.; Hofmann, H.; Li, J.; Ouyang, M. Sliding-mode and Lyapunov function-based control for battery/supercapacitor hybrid energy storage system used in electric vehicles. *Energy* **2017**, *122*, 601–612.
21. Hu, S.; Liang, Z.; He, X. Ultracapacitor-Battery Hybrid Energy Storage System Based on the Asymmetric Bidirectional Z-Source Topology for EV. *IEEE Trans. Power Electron.* **2016**, *31*, 7489–7498.
22. Peña-Alzola, R.; Liserre, M.; Blaabjerg, F.; Yang, Y. Robust design of LCL-filters for active damping in grid converters. In Proceedings of the 39th Annual Conference of the IEEE Industrial Electronics Society, IECON 2013, Vienna, Austria, 10–13 November 2013; pp. 1248–1253.
23. Inoue, S.; Akagi, H. A bidirectional dc–dc converter for an energy storage system with galvanic isolation. *IEEE Trans. Power Electron.* **2007**, *22*, 2299–2306.
24. Sun, J.; Grotstollen, H. Averaged modelling of switching power converters: Reformulation and theoretical basis. In Proceedings of the 23rd Annual IEEE Power Electronics Specialist Conference, PESC92, Toledo, Spain, 29 June–3 July 1992; pp. 1165–1172.
25. Li, Y.; Vilathgamuwa, D.M.; Loh, P.C. Design, Analysis, and Real-Time Testing of a Controller for Multibus Microgrid System. *IEEE Trans. Power Electron.* **2004**, *19*, 1195–1204.
26. Lo Brano, V.; Orioli, A.; Ciulla, G.; Di Gangi, A. An improved five-parameter model for photovoltaic modules. *Sol. Energy Mater. Sol. Cells* **2010**, *94*, 1358–1370.
27. Azzouzi, M.; Popescu, D.; Bouchahdane, M. Modeling of electrical characteristics of photovoltaic cell considering single-diode model. *J. Clean Energy Technol.* **2016**, *4*, 414–419.
28. Villalva, M.; De Siqueira, T.; Ruppert, E. Voltage regulation of photovoltaic arrays: Small-signal analysis and control design. *IET Power Electron.* **2010**, *6*, 869–880.
29. Messo, T. *Factors Affecting Stable Operation of Grid-Connected Three-Phase Photovoltaic Inverters*; Tampere University of Technology: Tampere, Finland, 2014.
30. De La Cruz, C.; Baptista Lema, M.; Del Toro, G.; Roncero-Sánchez, P. Energy Storage Integration with Renewable Energies: The Case of Concentration Photovoltaic Systems. *Handbook of Environmental Chemistry*; Springer International Publishing: Basel, Switzerland, 2016; Volume 34, pp. 73–94.
31. del Toro García, X.; Roncero-Sánchez, P.; Parreño, A.; Feliu, V. Ultracapacitor-based storage: Modelling, power conversion and energy considerations. In Proceedings of the 2010 IEEE International Symposium on Industrial Electronics, Bari, Italy, 4–7 July 2010; pp. 2493–2498.
32. Buller, S.; Karden, E.; Kok, D.; De Doncker, D.K. Modeling of the dynamic behavior of supercapacitors using impedance spectroscopy. *IEEE Trans. Ind. Appl.* **2002**, *38*, 1622–1626.
33. Zubieta, L.; Bonert, R. Characterization of double-layer capacitors for power electronics applications. *IEEE Trans. Ind. Appl.* **2000**, *36*, 199–205.
34. Roncero-Sánchez, P.; Acha, E. Design of a control scheme for distribution static synchronous compensators with power-quality improvement capability. *Energies* **2014**, *7*, 2476–2497.

35. Krause, P.C.; Wasynczuk, O.; Sudhoff, S.D.; Pekarek, S. *Analysis of Electric Machinery and Drive Systems*, 3rd ed.; Wiley-IEEE Press: New York, NY, USA, 2013.
36. Lu, D.; Zhou, T.; Fakham, H.; Francois, B. Ultracapacitor-based storage: Modelling, power conversion and energy considerations. In Proceedings of the 13th Power Electronics and Motion Control Conference, EPE-PEMC, Poznan, Poland, 1–3 September 2008; pp. 2142–2149.
37. Nise, N.S. *Control Systems Engineering*, 6th ed.; Wiley: Somerset, NJ, USA, 2011.



© 2018 by the authors. Licensee MDPI, Basel, Switzerland. This article is an open access article distributed under the terms and conditions of the Creative Commons Attribution (CC BY) license (<http://creativecommons.org/licenses/by/4.0/>).